Tampere University

Luukas Kuusela

DESIGNING OPTICAL GLASSES AND GLASS-CERAMICS FOR MID-INFRARED SENSING APPLICATION

Faculty of Natural Sciences and Engineering
Master of Science (Tech.)
June, 2020

ABSTRACT

Luukas Kuusela: Designing optical glasses and glass-ceramics for mid-infrared sensing application
Master's Thesis
Tampere University
Master's degree program in Science and Engineering
May 2020

The purpose of this thesis was to design new optical glasses and glass-ceramics that can be deposited to thin films to be used as a mid-infrared light source and waveguiding layer for sensing application. Thus, the goal was to develop new glass-based materials with strong emission at 2.7 μm, corresponding to the $^4I_{11/2} \rightarrow {}^4I_{13/2}$ transition of Er^{3+} under 980 nm laser excitation.

Erbium doped germanate glasses with the composition $\left(1-\frac{x}{100}\right)$*(64.6$GeO_2-10Ga_2O_3$-11.4BaO-9Na2O)-x$Er_2O_3$-5MO with MO=$Al_2O_3$, TiO_2, Y_2O_3 and ZnO and with x=0, 1 and 2.5 (in mol%) were prepared by the melt-quenching technique. The analysis of the IR spectra showed a high OH content in the glasses which is detrimental for MIR emission. Indeed, the OH groups in glass lead to a non-radiative relaxation route to quench the 2.7 μm emission. 2.7 μm emission was detected from all of the 2.5 mol% erbium containing glasses. The glass-ceramics were obtained by heat treating the glasses at T_g+20°C for 17 h to create the nuclei followed by a heat treatment at T_p for 1h and 6h for the growth of the nuclei into crystals. All of the glasses crystallized upon heat treatment. The crystallization mechanism was identified to be surface crystallization. The heat treatment increased the intensity of the emission of the Y containing glasses at 1.5 and 2.7 μm due to the crystalline field effect as evidenced by the sharp peaks in the emission bands. The Y containing glass had the most connected glass network, lowest OH content and highest 2.7 μm emission.

Electron beam physical vapor deposition was used to deposit thin film from the newly developed glass with MO=ZnO. The composition of the thin film was studied by X-ray photoelectron spectroscopy. Only Ge and Na were detected in the film. The original target and the deposited film were deemed unsuitable for the application, more deposition trials are needed to achieve thin films with similar luminescent properties as the target.

Keywords: germanate glass, thin film, laser glass, 2.7 μm emission

The Originality of this thesis has been checked using the Turnitin OriginalityCheck service.

TIIVISTELMÄ

Luukas Kuusela: Optisten lasien ja lasikeraamien suunnittelu keski-infrapunasensoreihin
Diplomityö
Tampereen yliopisto
Teknillis-luonnontieteellinen tutkinto-ohjelma
Toukokuu 2020

Tämän työn tarkoituksena oli suunnitella uusia optisia laseja ja lasikeraameja keski-infrapunasensoreihin. Nämä lasit ja lasikeraamit toimivat sensoreissa valonlähteinä ja aaltojohdekerroksina. Valonlähteinä toimimiseen laseilta vaaditaan suurta emissiointensiteettiä 2.7 µm:n alueella. Tämä emissio vastaa Er^{3+}-ionien elektronitransitiota tasolta $^4I_{11/2}$ tasolle $^4I_{13/2}$ 980 nm:n laserpumppauksen seurauksena.

Erbiumilla doupattuja germanaattilaseja valmistettiin koostumuksella $\left(1-\frac{x}{100}\right)$*(64.6$GeO_2-10Ga_2O_3$-11.4BaO-9$Na_2O$)-x$Er_2O_3$-5MO, missä MO=$Al_2O_3$, TiO_2, Y_2O_3 tai ZnO, ja x=0, 1 tai 2.5 mooliprosentteina. Lasit valmistettiin analyyttisen laadun kemikaaleista sulattamalla. Laseista mitatuista infrapuna-absorptiospektreistä havaittiin suuri hydroksyyliryhmäpitoisuus. Hydroksyyliryhmät laseissa vähentävät keski-infrapunaemission intensiteettiä, koska energiansiirto virittyneeltä tasolta hydroksyyliryhmälle mahdollistaa ei-radiatiivisen viritystilan purun. Suuresta hydroksyyliryhmäpitoisuudesta huolimatta 2.7 µm:n alueen emissiopiikki saatiin mitattua kaikista 2.5 mol% erbiumia sisältävistä laseista.

Laseja lämpökäsiteltiin 20 celsiusastetta niiden lasitransitiolämpötilan yläpuolella 17 tuntia ja tämän jälkeen pidettiin lasitransitiohuippulämpötilassa 1 tai 6 tuntia lasien kiteyttämiseksi. Kaikki lasikoostumukset pintakiteytyivät lämpökäsittelyiden myötä. Lämpökäsittely kasvatti yttriumia sisältävien lasien 2.7 µm:n ja 1.5 µm:n alueiden emissiopiikkien intensiteettejä. Emissiospektrien terävien piikkien vuoksi intensiteettien kasvamisen pääteltiin johtuvan kidekenttäefektistä. Tutkittujen lasien joukosta yttriumia sisältävien lasien lasirakenne oli linkittynein, niiden hydroksyyliryhmäpitoisuus oli pienin ja 2.7 µm:n alueen emissiointensiteetti oli suurin.

Elektronisuihkun avulla tapahtuvaa fysikaalista kaasufaasipinnoitusta käytettiin sinkkiä sisältävän lasin depositiointiin ohutkalvopäällysteeksi, minkä jälkeen ohutkalvon koostumusta tutkittiin röntgenfotoelektronispektroskopialla. Ohutkalvon koostumus erosi alkuperäisen lasin koostumuksesta. Ohutkalvossa havaittiin vain germaniumia, happea ja natriumia. Lisää depositiokokeiluja eri depositioparametreillä vaaditaan sensoriin soveltuvan ohutkalvon valmistamiseen.

Avainsanat: germanaattilasi, ohutkalvo, laserlasi

PREFACE

I would like to thank everyone involved in this thesis; my supervisor Associate Professor Laeticia Petit for her guidance and mentorship during my time in the Photonic glasses research group, Post-Doctoral researcher Alexander Veber and Doctoral researchers Mikko Hongisto and Nirjan Ohja for guidance and help with measurements, senior scientist Antti Tukiainen on his work on the MIR detection setup, Professor Mika Valden and his group for XPS measurements, Associate Professor Matthieu Roussey for thin film deposition experiments, and the rest of Photonic glasses group for advice and companionship.

I would like to extend my gratitude to the important people in my life. You have made me person I am today. I would like to thank my parents and my family, who have always been and who will always be there for me. My friends from high school and university have endured through exam weeks, assignments and also some fun times, you are irreplaceable. Also, thanks to Johanna for making our student apartment a home.

Tampere, 6 June 2020

CONTENTS

LIST OF FIGURES

LIST OF SYMBOLS AND ABBREVIATIONS

A.U.	arbitrary unit
ATR	attenuated total reflection
BGG	barium gallo-germanate
CVD	chemical vapor deposition
DTA	differential thermal analysis
DSC	differential scanning calorimetry
EDS	electron dispersive spectroscopy
ESA	excited state absorption
ET	energy transfer
ETU	energy transfer up-conversion
FTIR	Fourier transform infrared spectroscopy
GSA	ground state absorption
ICL	interband cascade laser
IMFP	inelastic mean free path
IR	infrared
MBE	molecular beam epitaxy
MCT	mercury cadmium telluride
MIR	mid-infrared
MRP	multiphonon relaxation process
NIR	near-infrared
NR	non-radiative decay
PLD	pulsed laser deposition
PVD	physical vapor deposition
QCL	quantum cascade laser
RE	rare earth
SEM	scanning electron microscopy
TIR	total internal reflection
UV-VIS	ultraviolet-visible
XPS	X-ray photoelectron spectroscopy

A	absorbance, Einstein coefficient
c	speed of light
C	concentration
d_p	penetration depth
e	electron charge
E	energy
ΔE	energy gap
ΔG	Gibbs free energy
h	Planck's constant
I	intensity
J	total angular momentum
L	angular momentum, thickness of glass sample
l	optical path length
m	mass
n	refractive index
N	ion concentration
P	probability
r	radius
S_m	line strength
S	spin
T	temperature

ΔT	temperature difference
$\langle \|\| U^{(\lambda)} \|\| \rangle$	double reduced matrix element of unit tensor operator
ν	frequency
λ	wavelength
$\bar{\lambda}$	mean wavelength
α	absorption coefficient
$\sigma(\lambda)$	absorption cross-section
β	branching ratio
ϵ	molar absorptivity
Ω_λ	Judd-Ofelt parameter
θ	angle
θ_c	critical angle
τ	lifetime
ω	angular frequency
ρ	density
ϕ	work function

°C	degrees Celsius (0 °C = 273.15K)
mbar	millibar (1 mbar = 100 Pa)
g	gram (1 g = 10^{-3} kg)
µg	microgram (1 µg = 10^{-6} g)
l	liter (1 l = 10^{-3} m^3)
cm	centimeter (1 cm = 10^{-2} m)
µm	micrometer (1 µm = 10^{-6} m)
nm	nanometer (1 nm = 10^{-9} m)
Å	ångström (1 Å = 10^{-10} m)
s	second
min	minute (1 min = 60 s)
h	hour (1 h = 60 min)
mol%	mole percent

Ar^+	argon ion
Al_2O_3	aluminum oxide
BCl_3	boron trichloride
Ba^{2+}	barium ion
BaO	barium oxide
CO	carbon monoxide
CO_2	carbon dioxide
Cu	copper
Er	erbium
Er_2O_3	erbium(III) oxide
Er^{3+}	erbium(III) ion
Fe	iron
Ga^{3+}	gallium(III) ion
GaO_4^-	gallium oxide ion
Ga_2O_3	gallium(III) oxide
Ge	germanium
Ge^{4+}	germanium(IV) ion
$GeCl_4$	germanium tetrachloride
GeO_2	germanium dioxide
GeO_6	germanium octahedra
Na_2CO_3	sodium carbonate

NO_2	nitrogen dioxide
O	oxygen
OH	hydroxyl group
$POCl_3$	phosphoryl chloride
$SiCl_4$	silicon tetrachloride
SiO_2	silicon dioxide
SiO_4^{4-}	orthosilicate ion
TeO_3	trigonal tellurite pyramid
TeO_4	trigonal tellurite bipyramid
TiO_2	titanium oxide
Y_2O_3	yttrium oxide
ZnO	zinc oxide
ZnSe	zinc selenide

1. INTRODUCTION

According to the World Health Organization (WHO), ambient air pollution is a major cause of death and disease. Air pollution was estimated to cause 4.2 million premature deaths per year in 2016. The air pollution-related deaths are caused by ischaemic heart disease, strokes, chronic obstructive pulmonary disease, acute lower respiratory infections and lung cancer. [1] This presents a need to develop compact and low-cost air pollution detectors.

The mid-infrared (MIR) region contains rotational and vibrational absorption peaks of molecular gases such as pollutants and greenhouse gases. CO, CO_2 and NO_2 have strong absorption peaks at 2.8 µm, 2.4 µm and 2 µm, respectively. The development of mid-infrared light sources enables the manufacturing of sensors which could be used for the detection and monitoring of air pollution from industry and aircrafts and the detection of narcotics and explosives for security scanning, among others. [2] On-chip optical devices offer numerous possibilities when sensors can be integrated into for example smartphones, tablets, and medical devices. On-chip integrated MIR sensing systems are based on attenuated total reflection (ATR) spectroscopy. [3] A typical MIR sensing system consists of a MIR light source, a waveguide structure and a MIR detector. If molecules are located at the waveguide surface within the penetration depth of the evanescent wave, the molecules can absorb a part of the light enabling the sensing of these molecules. The intensity of the evanescent wave can be increased by decreasing the thickness of the waveguide. [4] Thin film fabrication has advantages in the miniaturization of technology and reduction of energy and material consumption [5].

Erbium is a rare-earth (RE) element which possesses emission at 2.7 µm due to the $^4I_{11/2} \rightarrow {}^4I_{13/2}$ transition of Er^{3+} ions under 980 nm excitation, which can be realized by a commercially available high-power laser diode [6]. Glasses offer a great medium for light propagation and they can incorporate uniform distribution of RE [7 p.9]. Glass-ceramics can exhibit enhanced optical properties compared to glasses when the RE -ions are incorporated in a crystalline phase [8]. Therefore, erbium doped glasses and glass-ceramics are promising materials for MIR light sources and active waveguides.

However due to rather low energy of Er^{3+} $^4I_{11/2} \rightarrow {}^4I_{13/2}$ transition the radiative emission can be suppressed by multi-phonon relaxation if the glass has a high maximum phonon energy. [9] Therefore, low phonon energy glasses, which results in high mid-infrared

transparency, such as germanates and tellurites with maximum phonon energies of about 900 cm^{-1} and 700 cm^{-1}, respectively, are more suitable as host for MIR emission compared to for example well-known silicate glasses which have the maximum phonon energy of about 1100 cm^{-1} [10]. In addition to the low phonon energy, germanate glasses are of interest due to their superior thermal stability, mechanical strength and chemical stability compared to fluoride, chalcogenide, fluorophosphates and tellurite glasses. [11] For these reasons, germanate glass system was chosen for this study.

To use erbium doped glasses and glass-ceramics in on-chip integrated MIR sensing systems, they need to be deposited to thin films. Therefore, the purpose of this thesis is to design optical glasses and glass-ceramics that can be deposited to thin films to act as the mid-infrared light source and waveguiding layer for the sensing application. The thesis explains the full process of designing, preparing and analysing the glasses, glass-ceramics and thin films. To develop these materials, the composition-structure-property relation of these materials needs to be understood.

The necessary background information is discussed in Chapter 2. The basics of glasses and glass-ceramics: their definition, formation and structure are presented. Then laser glasses and the energy transfer mechanisms of rare-earth elements in laser glasses are discussed to understand the 2.7 µm emission of Er^{3+} ions. The basics of on-chip mid-infrared sensors and thin films are presented to understand the final application of the designed materials. Chapter 3 explains the experimental procedures used and how the glasses, glass-ceramics and thin films were prepared. The equipment used to study the samples and their working principles are briefly discussed. The parameters used for each experiment are presented. Chapter 4 contains the presentation and analysis of the gathered results. The effect of glass composition on the glass structure and properties is discussed. Then the effect of crystallization on emission properties is discussed and finally preliminary results on thin film deposition of the glasses are presented. The conclusions of the results are summarized in Chapter 5. Recommendations for future research are made based on the results of this work.

2. BACKGROUND

2.1 Glass

Glasses offer high homogeneity and the ability to be doped with various dopants such as rare earth ions. These properties among others make glasses favorable for optical and photonic applications. Categories of photonic glasses are gradient index glasses, non-linear optical glasses, laser glasses and magneto-optical glasses, just to cite a few.

There is a vast amount of different kinds of glasses with different compositions. This makes defining a glass somewhat difficult. However, all glasses can be described as non-crystalline solids which show a glass transition behavior. Glasses are often referred as amorphous solids, meaning they do not possess a long-range order but instead a short one. Figure 1 depicts the difference between a crystal and a glass.

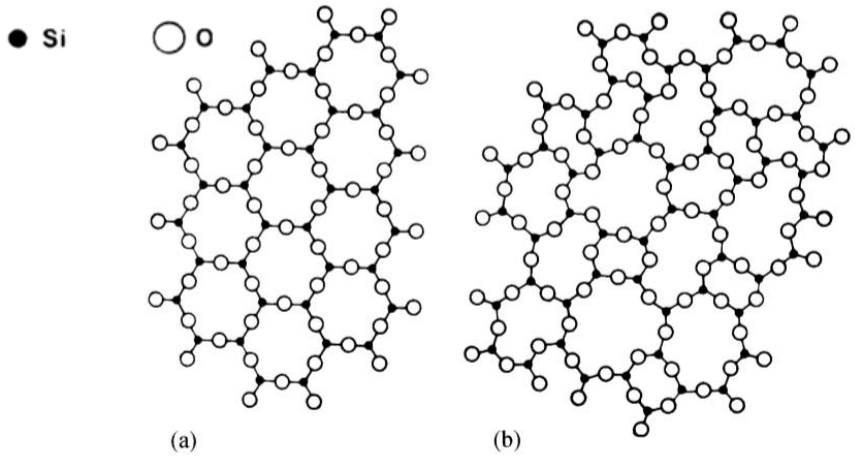

Figure 1. *Two-dimensional schematic of a SiO_2 a) crystal and b) glass.* [12]

As can be seen from Figure 1, the atomic arrangement differs between crystals and glasses. Unlike the crystals, the glass structure has no long-range periodic structure and lattice as the bond orientations vary especially. Glasses do not have a distinct melting point, but instead they start softening at a certain temperature. This is a consequence of the non-crystalline nature of glasses. [7, pp. 1-3]

The glass network is formed by the constituent known as network former. Additional components can be added to the glass. Some can replace network formers but cannot form glasses independently, these are known as intermediates. Others act as modifiers

by creating non-bridging oxygens. A schematic of a silicate glass modified by sodium is depicted in Figure 2.

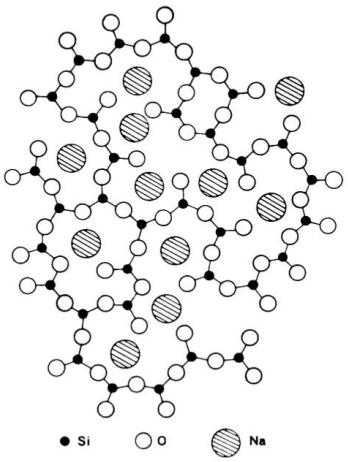

Figure 2. *Two-dimensional schematic of a sodium modified silicate glass.* [13]

As can be seen from Figure 2, the addition of modifier such as Na_2O leads to less connected network. Changing the glass composition changes the glass structure and so its properties making glass a very adaptive material.

Glasses can be molded into various forms and sizes enabling the manufacturing of devices such as glass fibers.

Glass is a great medium for light propagation. Indeed, there are no grain boundaries nor interference in the glass structure resulting to small scattering losses. Thus, glasses have high transparency between the absorption edges determined by the band gap energy and the vibration energy of the molecules. In practice, impurities such as bubbles or small crystals can act as scattering centers and need to be avoided in optical glasses in order to prepare transparent glasses. Also, compositional heterogeneity causes scattering losses. Impurities such as transition metal ions and water can cause absorption losses so eliminating these impurities is detrimental for the glass to be promising materials for most of the photonic applications. [7, pp. 9-11]

2.1.1 Glass formation

Glasses can be formed by various methods such as vapor phase oxidation processes (including modified chemical vapor deposition and outside vapor deposition) [7, p. 21], sol-gel technique [7, p. 25] and melt-quench technique [7 p. 16]. A schematic of glass formation is depicted in Figure 3.

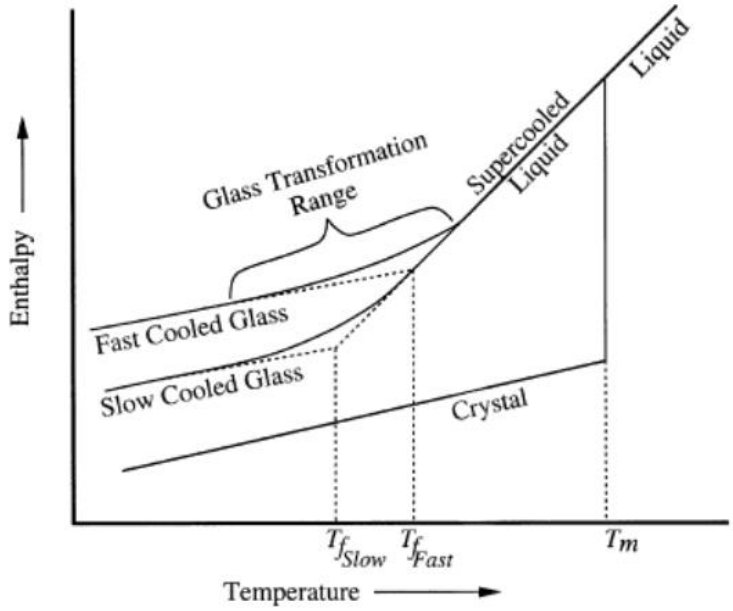

Figure 3. *Enthalpy-temperature diagram of the glass forming mechanism.* [14, p. 4]

When the temperature of a liquid is decreased to below its melting point, a phase transition usually occurs to a crystalline phase which is associated with an abrupt decrease in enthalpy. If the crystallization can be avoided, a supercooled liquid is obtained instead. As the temperature of the supercooled liquid is further decreased, the viscosity of the liquid increases. Gradually the viscosity becomes so high that the molecules cannot arrange to an ordered periodic structure and the structure becomes fixed. This is how a glass is formed. [14, pp. 3-5]

The described transition from a viscous liquid to a glass is known as glass transition and the corresponding temperature range is known as glass transition range. The glass transition temperature T_g is often determined using a differential thermal analyzer (DTA) or differential scanning calorimeter (DSC). The transition of a glass back to a viscous liquid happens if the glass is heated to a temperature above T_g. The increase of viscosity is dependent on the cooling rate of the liquid, so the glass transition temperature is also dependent on the cooling rate. As a low cooling rate allows better local arrangement of the molecules, it also affects the final enthalpy and the structure of the glass. This results in a lower glass transition temperature. Annealing of the glass near the glass transition temperature can be used to erase the thermal history of the glass and so its impact on the glass properties. [7, pp. 7-8]

2.1.2 Glass manufacturing techniques

Glasses can be prepared using different techniques such as for example:

- **The melt-quenching technique** was the first available method to produce glasses for practical applications [7, p. 16]. It is still the most widely used glass processing technique as the process is relatively quick, cheap and simple. It allows the production of innumerable compositions with numerous components. This method also allows the preparation of glasses with various shapes and sizes. In laboratory conditions a batch is prepared by mixing crystalline or amorphous raw materials in a mortar based on the desired glass composition. The batch is placed in a crucible which can be for example quartz glass, aluminum or platinum depending on the glass to prepare. The crucible is then heated in a furnace and the viscous glass melt is quenched meaning that the temperature is rapidly decreased. The quenching can be done in several ways depending on the glass forming tendency of the melt; the glass melt can be quenched in water, at room temperature or on preheated metal plate or for example in a mold to attain desired shape. Finally, the formed glass is often annealed to release thermal stress. [7, pp. 16-17]

- In the sol-gel technique, at first a sol is prepared. The desired constituents are well mixed into a liquid and undergo hydrolysis. After hydrolysis, the remaining liquid is called a sol. The sol is then dehydrated and condensation occurs into a wet gel. The gelling time can be decreased by adding an acid catalyst in the gel. The gel is then dried by evaporating the liquid. This step is done slowly to avoid fracturing the gel. Finally, the dried gel is sintered, densifying it into a poreless glass. Sol-gel method has many advantages over melt-quenching technique. The sintering temperature is significantly lower than that of a corresponding temperature needed in the melt-quenching technique. This enables the preparation of glasses with large amounts of dopants. The use of liquid precursors enables great purity through repeated distillations and avoids contaminations from a crucible. However, sol-gel method is time consuming. Additionally, the shrinkage of the wet gel often leads to fracturing and it is not applicable for all glass compositions. [7, pp. 25-27]

- Modified chemical vapor deposition is the most used method for the manufacturing of high purity silica fibers. $SiCl_4$ carried by oxygen is supplied to a rotating silica glass tube which is used as the cladding of the fiber. The tube is heated from the outside. The $SiCl_4$ gas reacts with oxygen and decomposes to form to SiO_2 glass particles which are deposited to the inner surface of the tube. The flow rate is computer

controlled by a gas supply system and additional dopants such as BCl_3, $GeCl_4$ or $POCl_3$ can be added in the tube to prepare silicate glasses. By controlling the dopant concentration, the refractive index of each glass layer can be tailored. A porous SiO_2 soot is obtained and dopants such as rare-earth ions can be added using solution impregnation by filling the tube with rare-earth containing solution or by gas phase doping. Finally, the deposit is dried to eliminate hydroxyl ions and other impurities such as Fe and Cu for example and then the tube is collapsed using heat to form a solid fiber preform. [15, pp. 234-235] Vapor phase oxidation processes enable the fabrication of glasses with very high purity especially regarding transition metal impurities. The chemical composition can be varied gradually or stepwise. These techniques however require dedicated instrumentation and the variety of glasses which can be fabricated is limited. [7, pp. 21-22]

2.2 Laser glasses

2.2.1 Lasing effect

Lasers are known as sources of monochromatic electromagnetic radiation with high intensity, coherence and directionality. Their operation is based on stimulated emission and the term laser originates from “Light Amplification by Stimulated Emission of Radiation” [16]. Lasers are key element of photonic technologies and they have a vast amount of applications in medical use, optical spectroscopy, processing of materials, optical communication, information processing and much more. [7, p. 82]

Population inversion needed for stimulated emission radiation can be achieved by optically pumping the lasing material. A three-level and a four-level lasing system are presented in Figure 4.

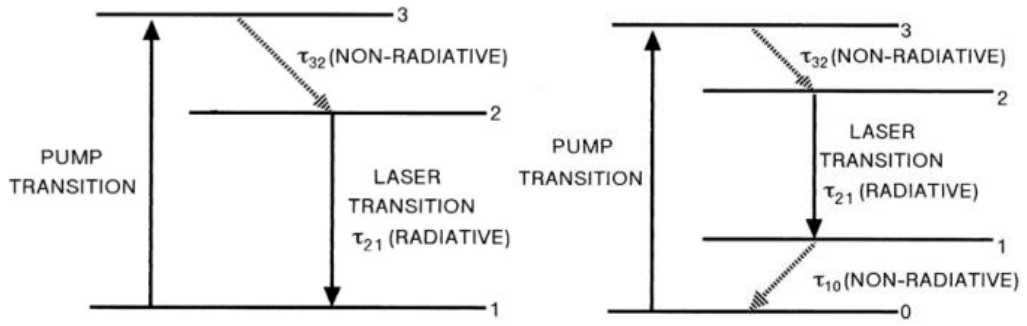

Figure 4. *Schematic picture of an optically pumped three-level (a) and four-level (b) laser system.* [7, p. 87]

The lasing material is pumped at some wavelength leading to the transition from the ground state to an excited level from which a non-radiative transition follows to a lower state and then to radiative laser transition, which is stimulated by passing light. This process can also be followed by another non-radiative transition to the ground level in the four-level system. [7, p. 87]

Laser applications set requirements for the properties of the materials used as an active media. They require strong absorption bands, high quantum efficiency of the emission and low intrinsic losses at a desired lasing wavelength. Such properties can be obtained by incorporating small amounts of rare earth (RE) ions of the lanthanide series, which have a partially filled *4f* electron shell, in a non-active transparent medium. The RE elements are presented in Figure 5.

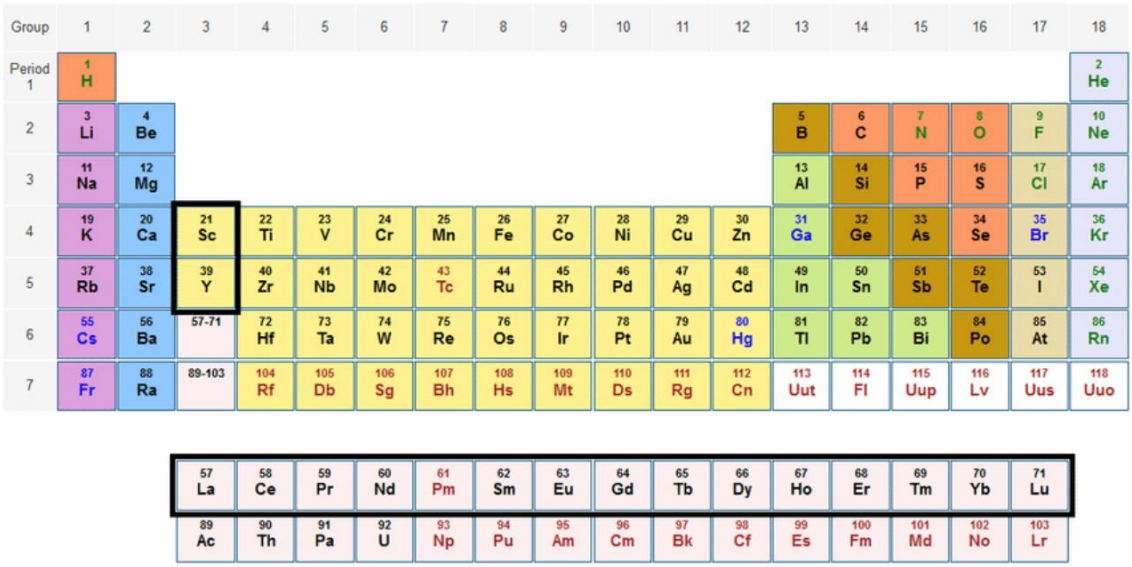

Figure 5. *The periodic table of elements. The RE elements are highlighted* [17].

The combination of Coulomb interaction and the spin-orbit interaction of electrons in an ion with large number of electrons arises a large amount of excited states suitable for optical pumping and fluorescent transitions. Due to inter-configurational origin of these transitions they result in sharp emission lines and high quantum efficiency. [7, p. 82]

Glasses can accommodate RE elements and ensure their uniform distribution in the medium and are therefore of interest. Additionally, the high transmission windows offered by glasses enable the excitation light of different wavelengths to be absorbed by the RE -ions rather than by the glass network. The same applies to emission, the luminescence at wavelengths is not absorbed by the glass. Glasses doped with RE -ions can be used as laser glasses. Laser glasses are commonly used in solid-state lasers and amplifiers, and the gain medium can be in form of a bulk glass, optical fiber or a waveguide.

2.2.2 MIR emission from Er^{3+} doped glasses

The schematic energy-level diagram of Er^{3+} is shown in Figure 6. Erbium is one of the most favorable RE -ions for an MIR, since it exhibits emission centered at 2.7 μm due to its $^4I_{11/2} \rightarrow {}^4I_{13/2}$ transition which can be obtained by excitation using a commercially available high-power laser diode emitting at 980 nm.

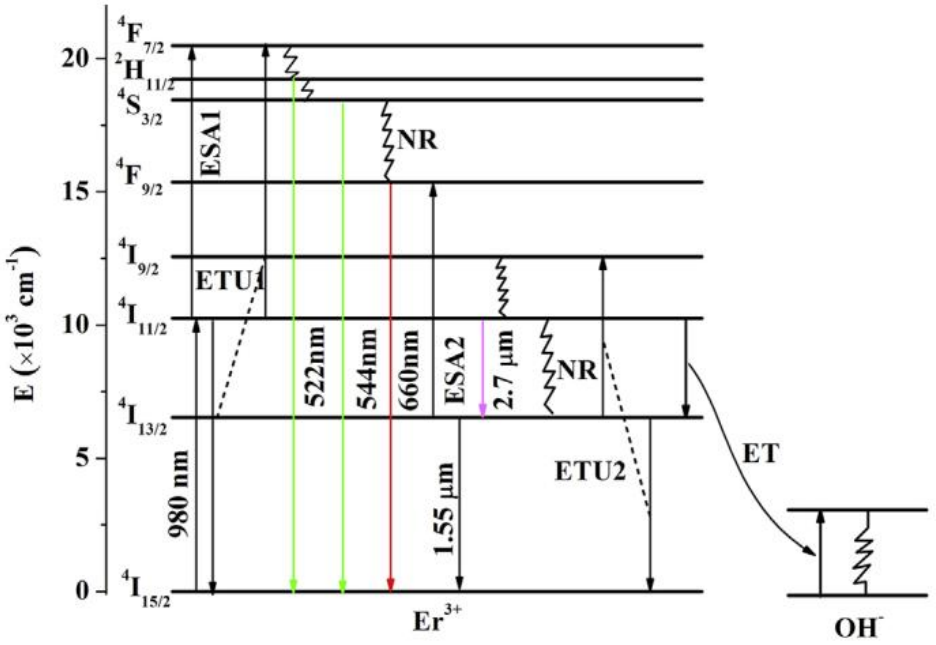

Figure 6. *Schematic energy-level diagram of Er^{3+} and the transitions possible under 980 nm excitation.* [6]

Under 980 nm pumping, the Er^{3+} ions are excited from the $^4I_{15/2}$ level to the $^4I_{11/2}$ excited state by ground state absorption. Back relaxation may happen in different manner:

- The $^4I_{11/2} \rightarrow {}^4I_{13/2}$ transition can be a radiative relaxation process leading to 2.7 μm emission or a non-radiative (NR) multi-phonon relaxation process.
- The $^4I_{13/2} \rightarrow {}^4I_{15/2}$ transition leads to an emission centered at 1.5 μm in a radiative relaxation.

If the concentration of Er^{3+} ions is large and/or the energy of the 980 nm excitation light is high, the ions could be further excited in different ways:

- The Er^{3+} ions can populate the $^4F_{7/2}$ by excited state absorption (ESA1) from the $^4I_{11/2}$ level or by an energy transfer up-conversion process (ETU1). The $^4F_{7/2}$ state can decay to the levels $^2H_{11/2}$, $^4S_{3/2}$ and $^4F_{9/2}$ through non-radiative relaxation processes. Three radiative emissions in the visible wavelengths correspond to $^2H_{11/2} \rightarrow {}^4I_{15/2}$ (522 nm), $^4S_{3/2} \rightarrow {}^4I_{15/2}$ (544 nm) and $^4F_{9/2} \rightarrow {}^4I_{15/2}$ (660 nm) transitions back to the ground state.
- The Er^{3+} ions can be excited from the $^4I_{11/2}$ state to $^4F_{9/2}$ through excited state absorption (ESA2). The population of $^4I_{11/2}$ and thus the 2.7 μm emission can be increased by an energy transfer up-conversion process (ETU2) followed by a non-radiative relaxation from the $^4I_{9/2}$ level. ETU2 is the major cause for concentration quenching in Er^{3+} doped glasses. When the Er-Er distance

decreases due to large amount of Er^{3+} ions, the probability for this interaction increases. [7, p.96]

It is important to emphasize, that the low energy of $^4I_{11/2} \rightarrow {}^4I_{13/2}$ transition responsible for the emission at 2.7 µm influenced by the phonon vibration of the host glass. [9] Achieving efficient emission at 2.7 µm requires the host glass to have a low maximum phonon energy since a low maximum phonon energy reduces the multi-phonon relaxation rate of the $^4I_{11/2}$ state and respectively increases the radiative relaxation route. [18]

Moreover, the presence of OH groups in the Er^{3+} doped material can add another non-radiative decay route from the coupling of the RE energy states and OH phonons. This is an important mechanism especially for Er^{3+} ions because the phonon vibration energy of OH is high and therefore two phonons are enough to cover the $^4I_{13/2} \rightarrow {}^4I_{15/2}$ transition. [8] The energy transfer (ET) process from Er^{3+} to OH can reduce especially the 2.7 µm emission that already competes with a non-radiative multi-phonon relaxation process [6].

2.2.3 Germanate glasses with low phonon energy

The table 1 list the maximum phonon energy of few glasses.

Table 1. *Maximum phonon energies of various glasses.* [10]

Glass	**Maximum phonon energy (cm^{-1})**
Borate	1400
Silicate	1100
Phosphate	1200
Germanate	900
Tellurite	700
Fluorozirconate	500
Chalcogenide	350

Germanate glasses are of interest due to their low phonon energy as compared to the well-known silicate glasses and other glasses. Germanate glasses possess also superior thermal stability and mechanical strength compared to fluoride, chalcogenide, fluorophosphates and tellurite glasses. Germanate glasses are also known for strong chemical stability and high mid-infrared transparency. [11]

Single-component GeO_2 glass consists of a three-dimensional network formed by randomly oriented Ge-O-Ge bonds [7, p. 31]. A Q^n notation is often used to describe the Ge(IV)-tetrahedral units, here n=0-4 is the number of bridging oxygens for the unit. A fully linked tetrahedron with four bridging oxygens is referred as a Q^4 unit and correspondingly, a single non-linked tetrahedron is referred as a Q^0 unit. [14, p. 84]

Barium gallo-germanate (BGG) glass is a multicomponent glass which due to a less crosslinked network has a higher rare earth solubility than the single-component GeO_2 glass [19]. The network structure of BGG glasses consists mostly of four coordinated Ge^{4+} and Ga^{3+} ions. The Ba^{2+} ions act as charge compensators on the GaO_4^- tetrahedra. The GeO_4 units are connected to either other germania units or to the GaO_4^- units. The network can also contain some GeO_6 octahedra. This multi-component glass has an enhanced durability, the durability of the glasses decreases with increasing GeO_2 content. [19] The glass forming region in BGG glasses is depicted in Figure 7.

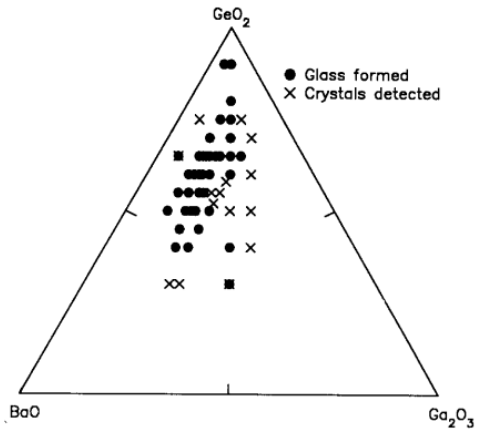

Figure 7. *Glass forming region in BaO-Ga_2O_3-GeO_2 system, compositions which crystallized are marked with X and those which formed glass with ●.* [19]

According to the study by Higby and Aggarwal [19],

- glasses in which the Ga_2O_3 / BaO ratio is smaller than one tend to crystallize. The excess of Ba^{2+} ions induces the presence of non-bridging oxygens in the network leading to a more disconnected network.
- when the Ga_2O_3 / BaO ratio is greater than one, the Ga^{3+} ions act as modifiers and they can be in coordination states other than GaO_4^- tetrahedra or in some sort of defect structure such as a tricluster.

2.7 µm emission from erbium has been reported in various types of germanate glasses: fluorotellurite-germanate [20], barium gallo-germanate [21] [22] and germanate based glass-ceramics [23]. In this study, GeO_2-Ga_2O_3-BaO-Na_2O glasses have been

investigated in order to develop a glass with strong MIR emission. Different network modifiers and intermediates were introduced to the BGG glass to find a suitable composition for good emission properties of Er^{3+} ions.

2.2.4 Glass-ceramics

Glass-ceramic is a material consisting of a glass and crystalline phases. Glass-ceramics have various applications even in our day-to-day lives; cookware, electric stovetops, construction materials, telescope mirrors, liquid crystal displays, solar cells and photonic devices [8] [14, p. 271]. Glass-ceramics offer various properties that are of interest: low thermal expansion coefficient, low dielectric constants, high electric resistivity, good machinability, biological activity, good mechanical strength, photosensitivity and non-linear optical behavior [7, p. 38] [8]. Additionally, glass-ceramics can exhibit enhanced optical properties compared to glasses. This enhancement can be achieved when the RE are incorporated in a crystalline phase. This can lead to a reduction in the inhomogeneous linewidth, to an increase in the emission and absorption cross-sections of the RE. The crystal phase can also have a low maximum vibrational energy. This reduces the probability of non-radiative relaxations from the excited states of the RE and consequently enhances the radiative decay routes. [8] [24]. An enhanced MIR emission of erbium has been reported when germanate glasses have been heat treated to form glass-ceramics [23].

Glass is a metastable state with a high free energy, in crystallization it transforms into an organized structure with lower energy. As a part of the glass transforms into the crystalline phase, the volume energy decreases as the crystalline phase has a lower energy. However, the creation of a new interface requires energy. The interaction of these energies as a function of the radius of the nucleus is presented in Figure 8.

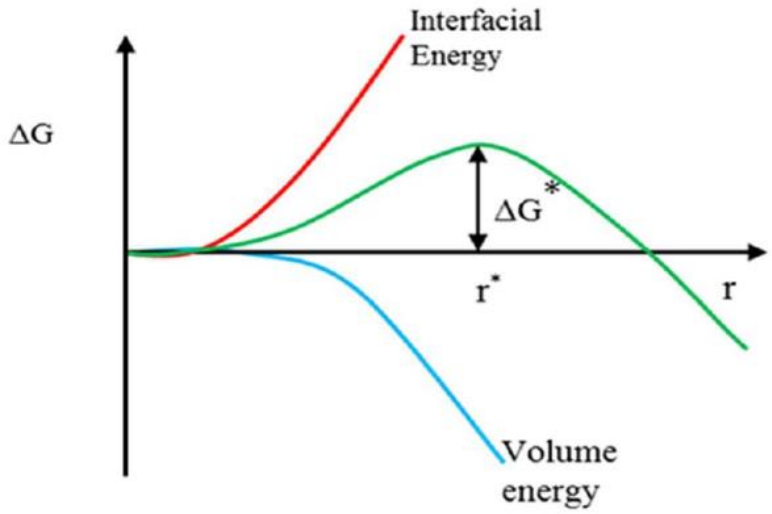

Figure 8. *Schematic of the interaction of the volume energy and interfacial energy as a function of the nucleus radius.* [25]

At small radius values, the interfacial energy term dominates and at larger values the decrease of total energy due to the volume energy term becomes dominant. A barrier energy ΔG^* corresponding to a critical radius r^* needs to be overcome to have stable nucleation. This is achieved by a controlled heat treatment of a glass material. [25]

To form a glass-ceramic, first a glass is formed using basic glass forming procedures explained in section 2.1.2. After annealing, the glass is heated to a temperature where nucleation of crystals occurs. Some glass compositions are self-nucleating and they undergo volume nucleation without external surfaces. However, the crystallization can also occur on external surfaces such as impurities or surface defects which act as nucleation cites. [8] This step determines the microstructure of the end product. A nucleation agent that can be for example a metal or a fluoride can enhance the crystallization. The nucleation agent provides a foreign surface for nucleation. [7] [14]

After nucleation, the glass is heated at high temperature and held there until a desired degree of crystallization is achieved. The relation between nucleation and crystal growth as a function of temperature is presented in Figure 9.

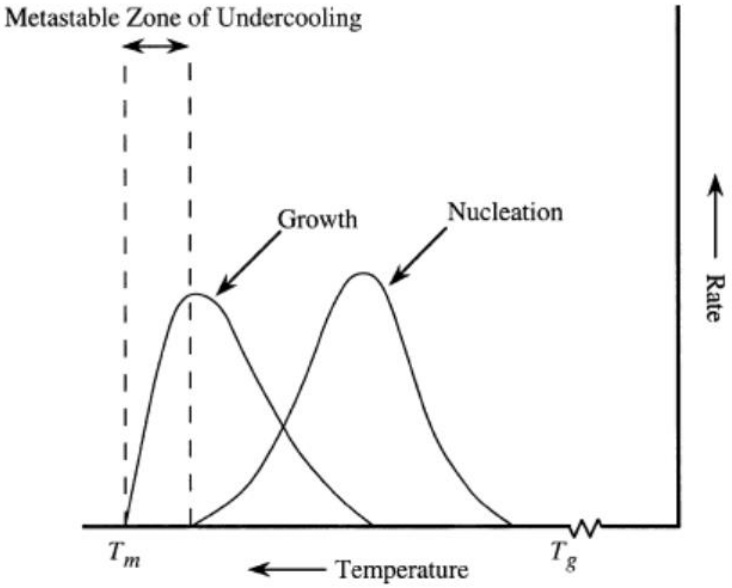

Figure 9. *Nucleation and crystal growth rates as a function of temperature.* [14, p.15]

To get a transparent glass-ceramic, nanocrystals with a size below 30 nm and a difference between the refraction coefficients of crystalline and glassy phases below 0.3 are needed [26]. The size and concentration of the crystals can be controlled by the heat treatment procedure: temperatures and periods of time of the heat treatment steps.

2.3 Thin films

Thin film technology is a growing field with various applications. Thin films have been utilized in thin film solar cells, high precision resistors, optical disks, magnetic memories, sensors, antireflection coatings and beam splitters among others. The utility of thin film technology comes from unique material properties originating from the atomic growth processes and quantum size effects due to the achieved small thickness.

Thin film fabrication has advantages in the miniaturization of technology and reduction of energy and material consumption. Additionally, it makes the use of toxic materials more plausible as only a very limited amount of material is needed.

2.3.1 Theory of film deposition

Thin films are fabricated by depositing material on a substrate. The thickness of the film is typically in the sub-micron range. Thin film deposition is done in four basic steps:

1. substrate preparation
2. creation or synthesis of the depositing material
3. transportation of the material from the source to the substrate
4. deposition onto the substrate and film growth. [27, p. 7]

Depending on the deposition process, these steps can be performed separately or simultaneously. The preparation of the substrate is an important part of the process as the substrate surface influences the properties, adhesion structure and surface texture of the deposited film. The substrate surface morphology and composition can be modified by means such as plasma treatment and reactive heat treatment.

Thin films can have various kinds of structures and compositions. A thin film can have a homogeneous composition, crystalline phase and microstructure, or it can consist of multiple layers or have a composite structure. A multilayer structure can be periodic, have a defined pattern or be completely random. Thin films can even have complex structures such as quantum dots, quantum wells, superlattices and nanowires. [27, pp. 7-8]

2.3.2 Techniques to deposit films

The properties of thin films are governed by the chosen deposition method. These methods can be classified into two categories: physical vapor deposition (PVD) processes and chemical vapor deposition (CVD) processes. [5]

- **In CVD** a volatile compound of the substance to be deposited is reacted with other gases or liquids to form nonvolatile reaction products. The solid reaction products are then deposited on to the substrate. CVD can be utilized to deposit a wide variety of materials by varying the composition and flow of the reaction gases. The advantages of CVD include large-area growth and high purity of the film. [5]
- **PVD** processes include electron-beam evaporation deposition, pulsed laser deposition, molecular beam epitaxy and sputtering among others. In PVD material from solid phase is transformed to vapor phase by different means and the thin film is deposited on a substrate by the condensation of the vapor. PVD is performed usually in vacuum and no chemical reactions are involved. The deposited material will be of the chemical composition of the vapor phase and can differ from that of the source composition. [5]

Pulsed laser deposition (PLD) uses a high-power pulsed laser to ablate or evaporate atoms from the target surface. The laser is absorbed at the surface of the target and the

material quickly evaporates from the surface. The evaporated material is then deposited on the surface of a substrate to form a thin film. To avoid the deposition of particles ejected from the target, the substrate is kept at an off-axis position. The advantage of PLD is that the target can be in different forms such as powder, sintered pellets and single crystal. However, PLD has a low energy conversion efficiency and the deposition of a film with uniform thickness is challenging as only a small part of the substrate is coated during each pulse. [28]

Sputtering deposition uses energetic ions to knock atoms or molecules from the target. The sputtering system consists of two planar electrodes, the cathode has the target material to be deposited and the substrate is placed on the anode. The sputtering chamber is filled with an inert gas, typically argon. A voltage is applied onto the electrodes and a glow discharge is initiated. The discharge ionizes the gas. The discharge generates Ar^+ ions, which are accelerated on the cathode and the sputtered material is deposited as a film onto the substrate. The gas density and pressure are controlled. The deposition rates of sputtering are lower compared to vacuum deposition methods such PLD and electron beam deposition. [29] Sputtering enables the deposition of a wide variety of materials including complex compounds [5].

Molecular beam epitaxy (MBE) is a method in which the evaporation rate of the source materials is *in situ* computer controlled. MBE can be used to fabricate high-quality ultrathin films with very sharp interfaces, controlled composition and microstructure. Ultrapure target materials are heated in effusion cells and sublimated, the produced molecular beams are then aimed at the substrate. The substrate is usually heated and rotated for uniform deposition. The process is done in ultrahigh vacuum. The drawback of MBE is the need for expensive and dedicated instrumentation. [30]

Electron beam deposition uses an electron beam to evaporate material from a target. The material in the vapor phase fills the chamber containing the substrate. The substrate is kept a lower temperature and material in the vapor phase is condensed onto the substrate forming a thin film. The method offers rapid deposition rate with a low consumption of energy. [31, pp. 400-403] The film obtained in this study were deposited using this technique.

2.3.3 Germanate thin films

Active germanate thin films have been successfully deposited using methods such pulsed laser deposition and sputtering [32-35]. Morea et al. reported Er^{3+} doped lead niobium germanate thin films on silicon substrates using pulsed laser deposition.

Doped and undoped glass targets were prepared and ArF excimer laser was used to deposit thin films. Metallic Er target was added to the chamber along with the undoped target to achieve *in situ* doped films. Both thin film structures exhibited similar persistent luminescence spectra at 1.5 µm. [32] Araújo et al. reported amorphous thin films produced by radio frequency sputtering from Yb_2O, Er_2O_3 and GeO_2-PbO glass with and without gold nanoparticle coatings. The sputtered thin films were made into rib waveguides by optical lithography followed by reactive ion etching process. Then gold target was radio frequency sputtered to layer one of the waveguides with gold nanoparticles. The waveguides exhibited luminescence under 980 nm laser excitation with the gold nanoparticle coated waveguide having enhanced luminescence compared to the non-coated waveguide. The waveguides were deemed strong candidates for integrated photonics. [33, pp. 131-143] Yoon et al. reported the deposition and characterization of Mn doped zinc germanate thin film on silicon substrate deposited using radio frequency sputtering. The thin film was confirmed to be amorphous as evidenced by the presence of a broad band in the XRD pattern of the film. Persistent luminescence measurements were performed to confirm luminescence from Mn in the thin film. [34] Xu et al. reported Bi, Ho singly doped and Bi/Ho co-doped oxyfluoride germanate thin films on silica substrates using pulsed laser deposition method. The prepared glass targets were deposited using a KrF excimer laser. XRD was used to confirm the amorphous structure of the achieved thin film and luminescence measurements were performed to confirm the luminescence of Bi and Ho in the thin films. [35]

2.4 Application of MIR materials

Mid-infrared (MIR) spectroscopy is of great interest for sensing applications as the excitation of vibrational and rotational transitions of various organic and inorganic molecules lie in this part of the electromagnetic spectrum. The MIR of various molecules is depicted in Figure 10.

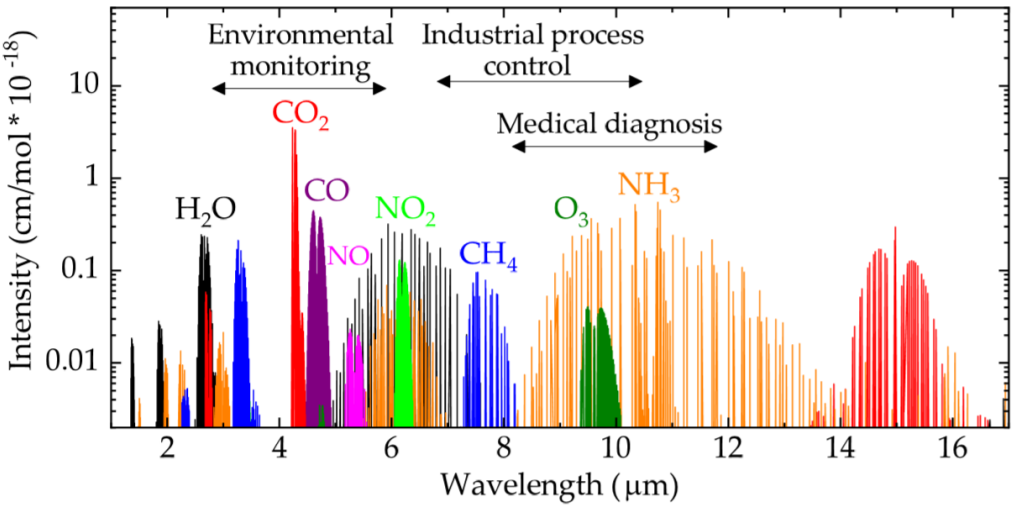

Figure 10. *Mid-infrared absorption spectra of various molecules.* [36]

These rotational and vibrational transitions enable sensitive and selective detection of molecules in liquid, gas and solid phases. [3] These kinds of sensors could be applied in fields such as gas detection, monitoring of pollutants, chemical and biological analysis, medical diagnostics and detection of chemical weapons, just to cite few applications.

2.4.1 Principle of sensing using MIR materials

The principle of sensing is based on attenuated total reflection (ATR) spectroscopy which enables enhanced sensitivity and the detection of samples that are too opaque for transmission absorption measurements. This technique is useful especially in case of biological applications. [3] ATR takes advantage of the total internal reflection (TIR) at an interface. In TIR, part of the electromagnetic field, an evanescent wave, attenuates through the interface with an exponentially decaying field. The condition for TIR requires that light is reflected at an interface with an incident angle exceeding the critical angle θ_c given by [31]

$$\theta_c = \sin^{-1}\left(\frac{n_c}{n_{wg}}\right), \tag{1}$$

where n_{wg} is the refractive index of the waveguide, n_c is the refractive index of the surrounding medium and the condition $n_{wg} > n_c$ is fulfilled.

The penetration depth of the evanescent wave at a given wavelength λ and incident angle θ is approximately [37]

$$d_p = \frac{\lambda}{2\pi\sqrt{n_{wg}^2 \sin^2\theta - {n_c}^2}}, \tag{2}$$

so the depth of the field can be tailored by the selection the waveguide material.

If molecules are located at the waveguide surface within the penetration depth of the evanescent wave, the molecules can interact with the evanescent wave. This leads to an absorption of light due to vibrational and/or rotational transitions of the molecules and consequently attenuation of the frequencies resonant with the transitions.

An IR-ATR absorption spectrum can be generated which in turn can be used to quantify the molecules. The evanescent field absorption follows a pseudo Beer-Lambert relationship given as

$$\log\left(\frac{I_0}{I}\right) = A = (\epsilon C l) r, \tag{3}$$

where I_0 is the intensity of the incident light, I is the intensity of the light after interaction with the molecules, A is the absorbance, ϵ is the molar absorptivity, C is the molecule concentration, l is the optical path length and r is the fraction of power guided outside the waveguide. [3]

The sensitivity and signal-to-noise ratio of the measurement is greatly affected by r and therefore by the intensity of the evanescent wave. The intensity depends on the dielectric constant at the interface, this in turn is affected by the materials, cross-sectional dimensions and thickness of the waveguide. The effect of waveguiding layer thickness and consequential need for thin films is depicted in Figure 11.

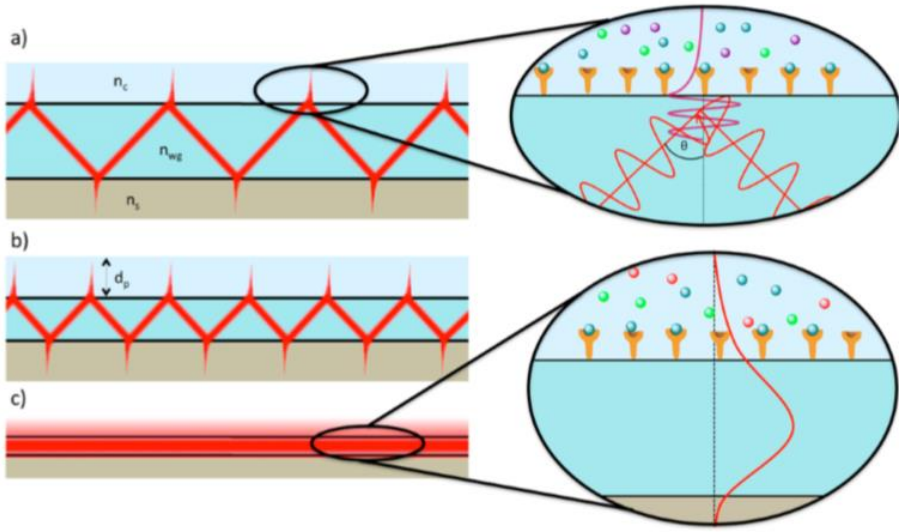

Figure 11. *The effect of layer thickness on the evanescent field behavior in a planar waveguide. a) The light propagates in a thick layer, b) number of total internal reflections increase along with decreasing thickness of the waveguide, c) with a small enough thickness, the evanescent field convolutes to a continuous field along the surface.* [4]

As the thickness of the waveguiding layer is decreased, the evanescent field behavior can be described as a continuous evanescent field instead of discrete penetration areas. This kind of structure is known as an integrated optical waveguide and the described behavior is achieved when the layer thickness is in the order of magnitude of the wavelength of the propagating wave. [4]

Laser light sources are of interest for on-chip MIR sensors as they offer a higher spectral density compared to broadband MIR light sources. A narrow emission band can be matched to a characteristic absorption band of a molecule to be detected. This enables a more compact and miniaturizable sensor with higher sensitivity while maintaining sufficient selectivity. [3]

A planar waveguide offering confinement of light along the vertical axis of the waveguide with respect to the direction of the propagating wave is known as a slab waveguide. Various thin-film waveguide geometries are depicted in Figure 12.

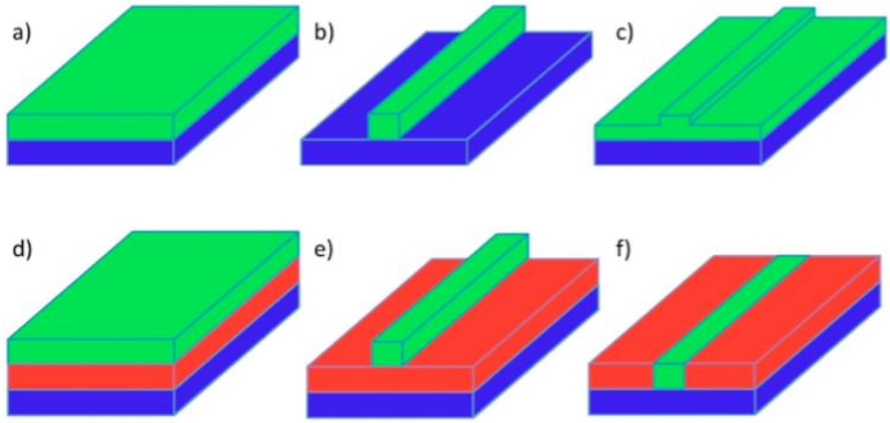

Figure 12. *Schematic of various thin-film waveguide geometries: a) slab waveguide, b) strip waveguide, c) rib waveguide, d) multilayer slab waveguide, e) ridge waveguide and f) buried/embedded waveguide.* [4]

Confining the light also in a horizontal axis further increases the fraction of the optical power in the evanescent field. This kind of tailored geometry further increases the sensitivity of the measurement. [4]

2.4.2 On-chip mid-infrared sensors

On-chip optical devices offer numerous possibilities when sensors can be integrated to for example smartphones, tablets, and medical devices. On-chip integration would offer application such as breath, body tissue and fluid analysis as well as food quality control and detection of contaminants and air pollution. [38] Integrated and even on-chip MIR sensing technology is a promising field for ongoing research. The possibility of on-chip integration of optical sensors has already been demonstrated in ultraviolet-visible (UV-VIS) and near-infrared (NIR) sensing technology. Currently the dimensions of IR spectroscopic equipment limit the application possibilities. [4]

A typical MIR sensing system consists of a MIR light source, a waveguide structure for the propagation of the IR light often also acting as the active optical transducer and of some sort of MIR detector. Quantum cascade lasers (QCL) and interband cascade lasers (ICL) are considered the most advanced available MIR light sources. [4] They are however expensive and have high power consumption [38]. The MIR waveguides used for sensing applications are usually fabricated from a limited group of MIR transparent materials consisting mainly of polycrystalline silver halides, tellurium halides and amorphous chalcogenide glasses. [4] There is a need for the development of new MIR light sources and waveguides.

Germanium based waveguides have been used in MIR spectroscopy due to their broad transparency in the MIR, nontoxicity and silicon process combability [39] [40]. Germanium has typically been used as a single crystalline waveguide. Germanium waveguide on ZnS substrate was reported already in 1997 [41], germanium prisms were polished to a thickness of 30 µm and evanescent-wave absorption from water droplets was demonstrated. Chang et al. demonstrated a low loss monocrystalline on-chip germanium waveguide on a silicon substrate [39]. Reduced pressure chemical vapor deposition was used to grow a germanium layer onto the substrate and photolithography was utilized to obtain high-quality single mode strip waveguides. The waveguide was then integrated with a microfluidic chip to demonstrate the on-chip capabilities by cocaine detection. The measurement setup used by Chang et al. is presented in Figure 13.

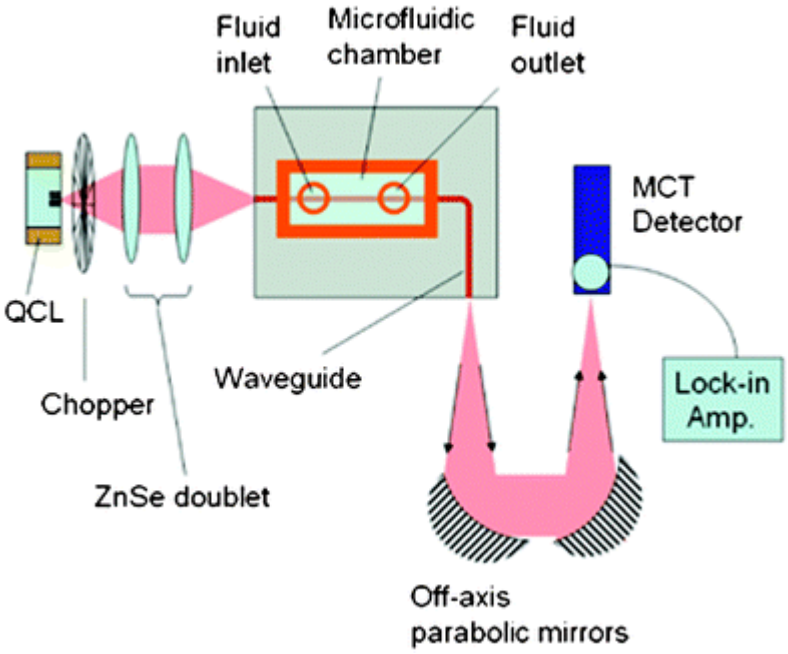

Figure 13. *Measurement setup used by Chang et al. to demonstrate cocaine detection by a mid-infrared germanium waveguide microfluidic chip.* [40]

The system used an QCL source coupled to the waveguide by a ZnSe doublet and utilizing a mercury cadmium telluride (MCT) detector. The system was capable of detecting cocaine dissolved in tetrachloroethylene with the concentration as low as 100 µg/L.

3. EXPERIMENTAL WORK

3.1 Sample preparation

3.1.1 Glass melting

Glasses of the composition $\left(1-\frac{x}{100}\right)$*(64.6$GeO_2-10Ga_2O_3$-11.4BaO-9$Na_2O$)-x$Er_2O_3$-5MO with MO=$Al_2O_3$, TiO_2, Y_2O_3 and ZnO and with x=0, 1 or 2.5 (in mol%) were prepared by the melt-quenching technique. The samples are referred as 0ErAl, 0ErTi, 0ErY and 0ErZn when x=0, 1ErAl, 1ErTi, 1ErY and 1ErZn when x=1, 2.5ErAl, 2.5ErTi, 2.5ErY and 2.5ErZn when x=2.5.

The following analytical grade powder raw materials were used to prepare glasses: GeO_2 from Sigma-Aldrich, ≥99.99% purity; Ga_2O_3 from Sigma-Aldrich, ≥99.99% purity; BaO from Sigma-Aldrich, ≥99.99% purity; Na2CO_3 from Sigma-Aldrich, ≥99.8% purity; Er_2O_3 from Sigma-Aldrich, ≥99.99% purity; Al_2O_3 from Sigma-Aldrich, ≥99% purity; TiO_2 from Sigma-Aldrich, 99.8% purity; Y_2O_3 from Alfa Aesar, 99.9% purity and ZnO from Sigma-Aldrich, 99.99% purity. The powders were weighed using an OHAUS Adventurer Analytical -scale, with the accuracy of 0.001 g. Then the powders were mixed and grinded in a mortar to improve the homogeneity of the glass batch. The crucible with the batch put in a platinum crucible was placed in the furnace at room temperature and then heated up to desired melting temperature using 15°C/min heating rate. The glasses were melted at either 1450°C (MO=Al_2O_3 or ZnO) or 1550°C (MO= TiO_2 or Y_2O_3) for 40 min using an electric furnace in air. During the melting process the melt was mixed at the 20-minute mark and finally quenched at the 40-minute mark on a metal plate. The glasses were annealed at 400°C for 5 h to remove thermal stress caused by the quenching. After annealing, the glasses were polished for optical measurements.

To form the glass-ceramics, the glasses were heat treated at 20°C over their glass transition temperature for 17 h to create the nuclei and at their crystallization peak temperature for 1 h and 6 h for the growth of crystals. The experiments were conducted in air using 15°C/min heating rate.

3.1.2 Thin film deposition

The film obtained in this study were deposited using electron beam physical vapor deposition as this technique has been utilized for the deposition of a wide variety of materials and it has a rapid deposition rate with a low consumption of energy. [29] A typical electron beam deposition system is depicted in Figure 14.

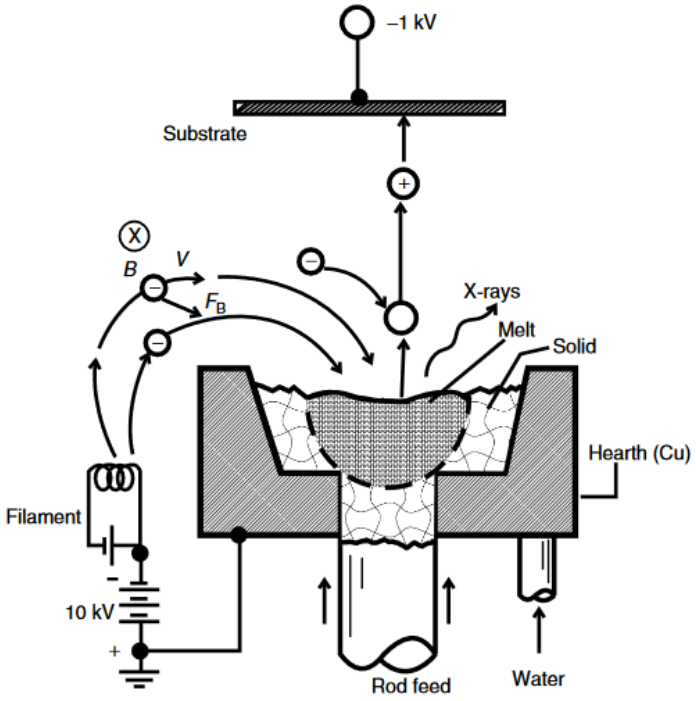

Figure 14. *A schematic of a typical electron beam deposition system.* [29, p. 401]

Electrons are generated at a filament which is kept out of the way of the evaporating material. An electromagnetic field is used to accelerate the electrons from the cathode source and focus them onto the target surface. When the accelerated electron hit the target surface, the kinetic energy of the electrons is converted to mostly thermal energy. The thermal energy is used to melt or sublimate the target material to produce the vapor phase. The highest temperature in the system is limited to a small area at the target surface. Electron beam systems require a vacuum to avoid contamination from air. The chamber is kept at a low pressure to avoid the collision of the evaporated molecules with each other. Therefore, the molecules do not lose their energy before deposition. [29, pp. 400-403] One should keep in mind that when depositing complex compositions, attaining a uniform layer of the same composition as the target is difficult. The composition of the

target material and the deposited film can differ and therefore characterization of the film is required after deposition. [29, pp. 410-412]

Glass targets of the 1ErZn and 2.5ErY compositions were prepared using similar melting procedures as described in 3.1.1. The glasses were quenched in a mold to prepare flat disks with 2.6 cm diameter and 3.5 cm thickness. Thin film deposition trials were performed on fused silica substrates. For both trials the substrate was cleaned using acetone to remove organic impurities, then rinsed in isopropanol to remove residual acetone and other impurities and finally rinsed in water. Then the substrate was dried using N_2 gas and treated by oxygen plasma for 1 min to remove any residual molecules. The evaporator was pumped down to 0.02 mbar vacuum and the target was evaporated by gradually increasing the electron beam hitting it. The rate of evaporation fluctuated between negative and positive values. The calculated density used for the evaporation process was 4.615 g/cm^3 and the tooling factor used was 100 %.

The film deposition was performed in collaboration with Associate Professor Matthieu Roussey from the University of Eastern Finland.

3.2 Glass density

Archimedes' method was used to determine the density of the glasses. A schematic of the process is presented in Figure 15.

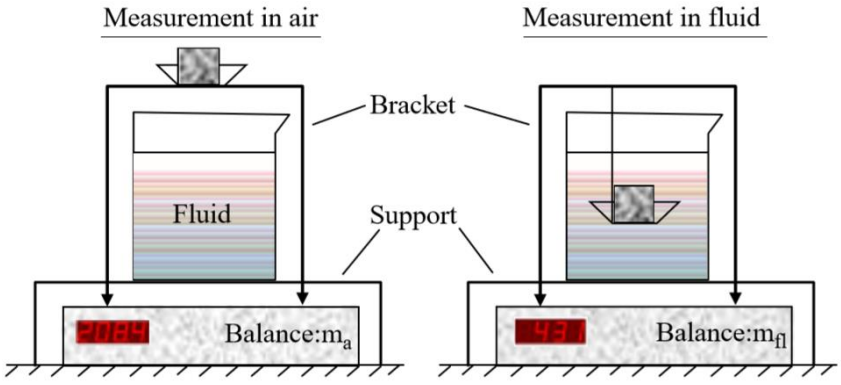

Figure 15. *Schematic of Archimedes' method to determine density of a solid.* [42]

The Archimedes' method is based on the buoyancy force caused by a solid being submerged in the liquid. The solid is weighed in air and in an immersion liquid. The density can be determined as

$$\rho_{sample} = \rho_{fl} \frac{m_a}{m_a - m_{fl}}, \quad (4)$$

where ρ_{sample} and ρ_{fl} are the densities of the sample and the fluid in which the sample is immersed, respectively, m_a is the measured reading in air and m_{fl} is the measured reading in the fluid.

The density of the fluid is temperature dependent, therefore the temperature of the fluid is measured to determine the density of the fluid. Here the buoyancy of air is neglected as its effect on the accuracy of the measurement is small. [42]

The density of the glasses was determined using an OHAUS Adventurer Analytical - scale using the dedicated density measurement kit for the scale. Ethanol was used as an immersion liquid. Each glass was weighed independently two times both in air and in the immersion liquid to verify that the results are within the accuracy of the measurement. The estimate for the accuracy of the measurement is ± 0.02 g/cm^3. Any trapped gases escaping during the immersion would be seen as bubbles in the immersion liquid and could affect the measurement accuracy. Therefore, the glasses were polished prior to the measurement to have less bubbles trapped on the surface of the glass.

3.3 Thermal properties

The thermal properties of glasses are of importance to understand the behavior of glasses when the temperature is increased. Differential thermal analysis (DTA) is a useful technique to determine the thermal properties of glasses such as the thermal stability of the glass against crystallization as well as the temperature at which the glass starts softening. DTA is a very useful technique for various reasons:

- measurements can be performed sufficiently quickly,
- the analysis of the DTA data is straightforward,
- it only requires a small amount of glass and,
- it is suitable for all glass systems. [43]

In DTA, the studied sample and an inert reference sample are placed in a DTA cell which contains temperature sensors and the equipment to heat the samples. The basic principle of DTA is to obtain information of thermal changes in a sample by comparison to an inert reference material which is heated alongside the sample. Two sensors are used, one is connected to the sample and one to the reference. As the samples are heated using an identical temperature program controlled by a computer, the difference between the response of the measuring sensors is gathered. A difference in temperature is perceived when the measured sample undergoes thermal events such as phase transitions, glass transformation or crystallization. Measuring the difference in

temperature allows the signal to be independent of thermal effects which affect both the sample and the reference. The results from the experiments are displayed as a thermal analysis curve, also known as a thermogram, in which the heat flow is plotted against the temperature of the sample. If the direction of the curve is upwards, the sample is releasing energy in an exothermic reaction, correspondingly if the heat flow curve is decreasing the sample is undergoing an endothermal reaction. [44] A typical thermogram of a glass is presented in Figure 16.

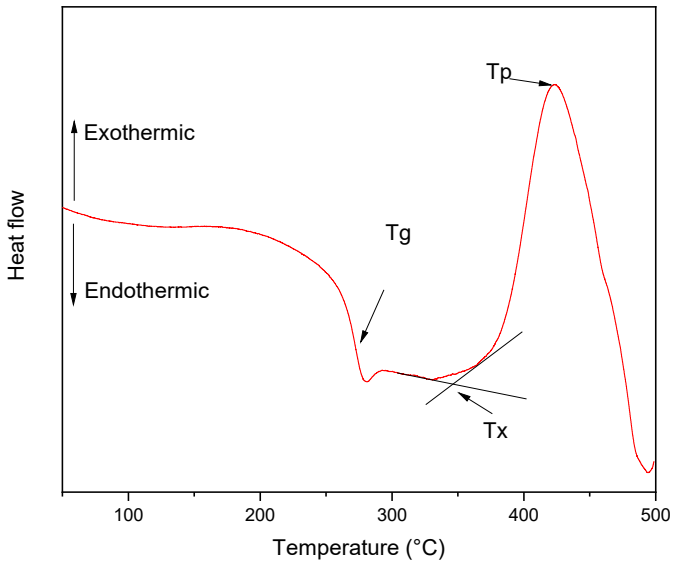

Figure 16. *Typical thermogram of a glass sample with markings for characteristic temperatures.*

The thermal properties of glasses are characterized by a set of temperatures: the glass transition temperature (T_g) and the crystallization temperatures (T_p and T_x).

- T_g is the temperature where the glass viscosity is equal to 10^{12} (Pa·s). It is often used to determine the temperature for annealing the glass and for the temperature to be used for the nucleation of crystals. T_g is determined as the inflection point of the endotherm, in practice it is often determined from a minimum of the derivative in the thermogram.
- The crystallization temperatures are needed to determine the temperature of heat treatment to grow the nuclei into crystals. T_p is determined as the maximum point of the first exothermic peak and T_x as the onset point of the peak.

$\Delta T = T_x - T_g$ is often used to evaluate the thermal stability of the glass against crystallization. The glass is considered to be thermally stable if ΔT is larger 90ºC. If ΔT < 90ºC, crystallization might occur during the glass processing (fiber drawing, film deposition).

The thermal properties of the glasses were measured using a Netszch F1 instrument. Glass samples were crushed into powder and heated using a 10°C/min heating rate in the range from 30°C to 1100°C. A platinum pan was used for the measurement. The accuracy of the measurement is $\pm$3°C.

3.4 Structural properties

Understanding the structure of a glass is detrimental to understand how the glass properties depend on the glass composition. Techniques such as Raman and infrared spectroscopies are commonly used to study the glass structure. Usually Raman active vibrations cannot be infrared active and vice versa. For this reason, IR and Raman spectroscopies are complimentary methods to study the structure of solids. [45, pp.31-32]

3.4.1 Raman spectroscopy

When electromagnetic radiation is scattered from an atomic or molecular sample, the wavelength of radiation remains unchanged for the most part. This kind of scattering is known as Rayleigh scattering. If the wavelength of a scattered photon is different than that of the incident photon, the photon is Raman scattered. This phenomenon is the basis for Raman spectroscopy. [46, p. 122]

There are two different types of Raman scattering. These Raman scattering processes are depicted in Figure 17.

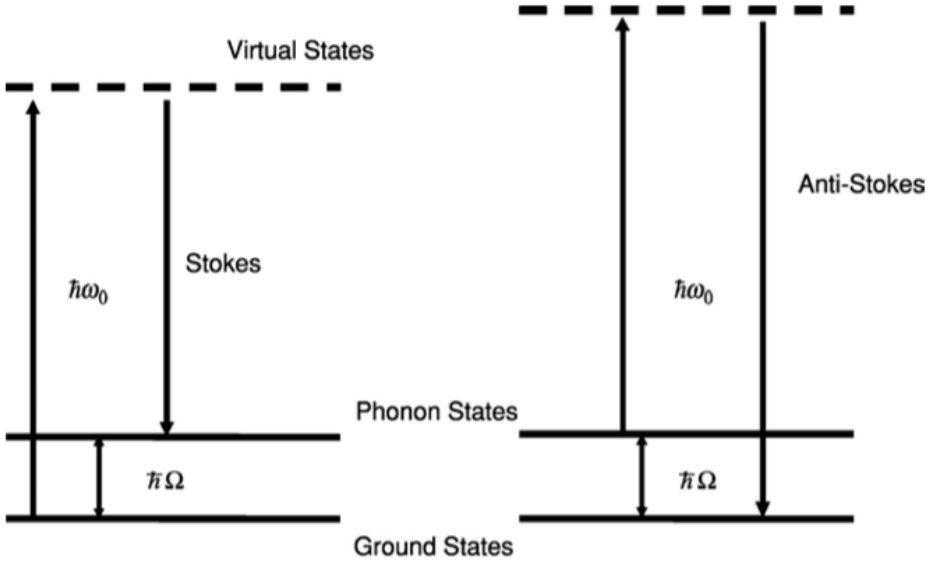

Figure 17. *Energy level diagram of Raman scattering processes, a) Stokes and b) Anti-Stokes.* [45, p. 32]

In Stokes Raman scattering, an incident photon with energy $\hbar\omega_0$ is absorbed resulting in an excitation from the ground state to a virtual excited state. The excitation is released by an emission of a photon, leaving the system in a phonon-excited state. Correspondingly, in anti-Stokes Raman scattering, a system in a phonon-excited state absorbs a photon which excites it to a virtual state and an emission to the ground state follows. As the phonon energy states are characteristic, Raman spectroscopy enables the identification of vibration modes making it a useful method to study the structure of a solid. [45, pp. 31-32]

The excited virtual states do not correspond to real eigenstates of a system, consequently the probability for Raman scattering is low. Compared to fluorescence spectra involving electronic eigenstates, Raman spectra are weaker by a factor of about 10^{-5}-10^{-7}. [45, pp 31-32] The low scattering probability is problematic as Raman signal can be masked by fluorescence of the sample.

A schematic of a typical Raman setup is depicted in Figure 18.

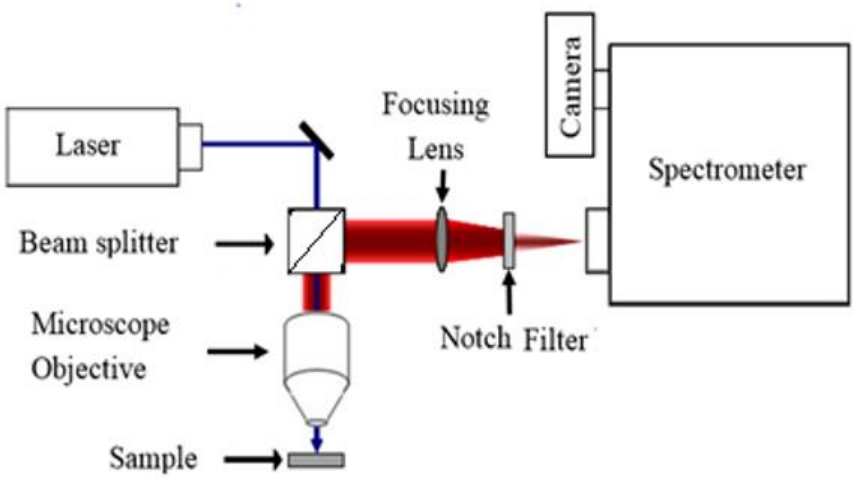

Figure 18. *A schematic of a Raman spectrometer.* [47]

In Raman spectroscopy, a laser is focused at the sample, the Raman scattered photons are detected and a spectrum is gathered. The difference in energy between the incident laser beam and Raman scattered light is rather low, also the probability for Raman scattering is low, thus a highly monochromatic, powerful light source is needed to have an interpretable Raman spectrum. These qualities are combined in lasers, making them the most suitable light source for Raman spectroscopy. The dominating Rayleigh scattering is filtered out using a notch filter before the scattered light passes through a monochromator and a spectrum is gathered. A high efficiency low noise CCD camera is commonly used today for detecting the Raman signal. [45, p. 32]

In this study, the Raman spectra of as-prepared glasses were measured in the 150-1200 cm^{-1} range using an inVia™ Qontor® confocal Raman microscope (Renishaw, Gloucestershire, UK) using a 405 nm laser at room temperature.

3.4.2 FTIR spectroscopy

Absorption of light in the infrared region corresponds to transitions between vibrational states in a molecule. The vibrational energy level spacings are characteristic to molecules and therefore absorption in infrared can be used to study the structure of a sample. [46, pp. 166-167] The method known as Fourier transform spectroscopy provides various advantages over traditional dispersive spectroscopy techniques. Fourier transform infrared (FTIR) spectroscopy is based on using a broadband light source instead of a monochromatic beam. The light frequencies are modulated and using Fourier transformation the absorption or transmission spectrum is generated.

A typical FTIR spectrometer is depicted in Figure 19.

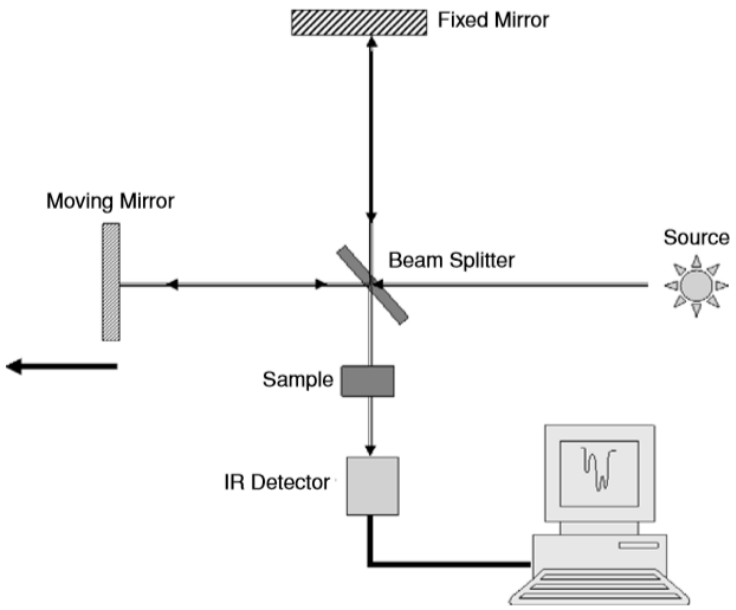

Figure 19. *A schematic diagram of an FTIR spectrometer.* [45, p. 33]

In an FTIR measurement, the light source is shined on a beam splitter splitting the beam to two different mirrors, one of which is stationary and the other one is permanently oscillating in a controlled way. The beams reflected from the mirrors combine at the beam splitter and pass through the studied sample before passing to the detector. This kind of measurement setup is known as the Michaelson interferometer. Depending on the position of the moveable mirror, the recombining light beams can experience

- constructive interference arriving to the sample at the same phase which is seen as a maximum at the detector,
- destructive interference arriving at the opposite phases and seen as a minimum at the detector,
- or something in between.

An interference pattern known as an interferogram is gathered. The interferogram is converted to a spectrum by a Fourier transformation utilizing mathematical manipulation. Usually a reference measurement is made without a sample, then an interferogram is measured with the sample in place and finally the transmittance spectrum is generated. [45, pp. 33-36]

Compared to dispersive techniques, FTIR has many advantages originating from the use a light source containing various wavelengths without using a monochromator. FTIR

provides a better signal-to-noise ratio. FTIR also provides a high resolution which is constant over the spectral range. [45, p.36]

Attenuated total reflection can be used in conjunction with FTIR spectroscopy. ATR utilizes the total internal reflection at an interface to generate an evanescent wave which penetrates a few micrometers to the studied sample. A schematic of an ATR setup is depicted in Figure 20.

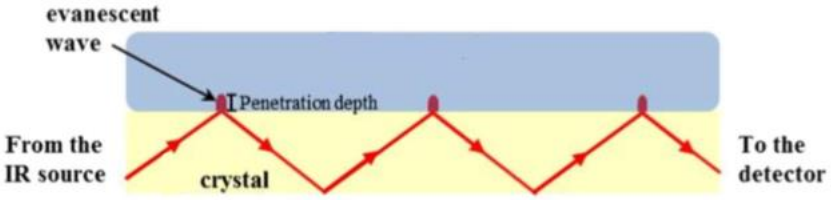

Figure 20. *A schematic diagram of an ATR setup.* [48]

IR light from the source is aimed at a high refractive index crystal in an angle so that the total internal reflection is achieved. The transmittance of the evanescent wave is measured and the transmittance spectrum is generated. [48]

OH groups have a strong and broad absorption band in the IR region and so the IR transmittance spectrum of a glass can be used to estimate the amount of OH groups present in glasses. The amount of OH groups can be determined as follows:

$$N_{OH} = \frac{N}{\epsilon L} ln\left(\frac{1}{T}\right), \tag{5}$$

where N is the Avogadro constant, L is the thickness of the sample, T is the measured transmittance at the measured peak absorption coefficient in the IR and ε is the molar absorptivity of free OH groups in a corresponding glass. Using the molar absorptivity in silicate glasses $\epsilon = 49.1x10^3$ cm^2/mol is a sufficient approximation. [49]

The as-prepared glasses were crushed into a powder and an FTIR spectrometer (PerkinElmer Spectrum One FTIR) with ATR mode was used to measure the IR spectra of the glasses in the 650-1500 cm^{-1} region**.** FTIR spectrometer was also used to measure the transmittance spectra in the 1500-8000 cm^{-1} region of polished glass samples to determine the OH content of the glasses.

3.5 Optical properties

The glasses interaction with light is one of the key features to be tailored in glasses for photonic applications. Absorption and emission spectra can be used to gather

information about properties such as position of absorption gap, changes in the site of RE in the glasses and absorption cross-sections.

3.5.1 UV-VIS-NIR absorption

The absorption spectra of glasses in the ultraviolet (UV), visible (VIS) and near-infrared (NIR) ranges give important information on the optical and structural properties of the glasses. The absorption in UV is due to charge-transfer transitions, and in a stronger glass network the absorption edge is at a higher energy which corresponds to lower wavelengths. Thus, the position of the UV absorption edge gives information about the strength of the glass network. The absorption cross-section is affected by the site of the RE and therefore changes in the absorption spectra give information about the local environment changes of the RE.

The absorption spectra of the glasses in the UV-VIS-NIR were measured using a grating spectrometer. A schematic diagram of a typical spectrometer is depicted in Figure 21.

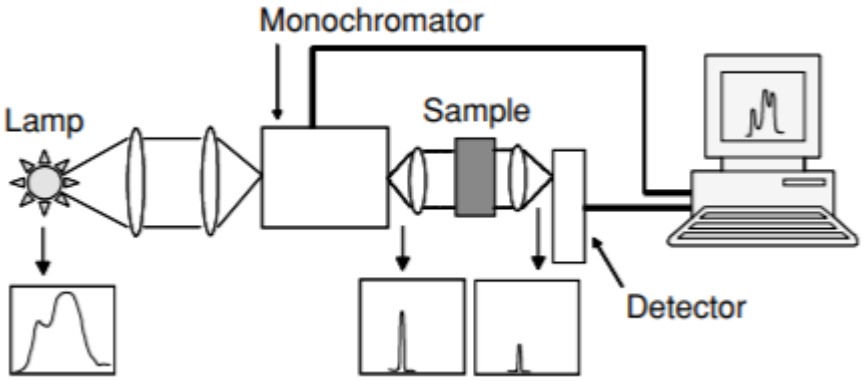

Figure 21. *A schematic diagram of a typical spectrometer.* [45, p.12]

In a spectrometer, some light source is used to get a broad spectrum range of light. For the UV range, a deuterium lamp is often used and for the visible and NIR ranges a tungsten lamp is used. A monochromator is used to select a single wavelength of light at a time and a detector, often photomultiplier, is used to record the light intensity. A reference spectrum is gathered before placing the sample on to a sample holder on the path of the light. The spectrum passing through the sample is then gathered and the amount of light passing through the sample is compared to the reference intensity. As light is absorbed by a material, the number of photons and consequently the light intensity decreases. The difference in intensity can be used to determine how much of the light is absorbed by the sample material. [45, pp. 11-12]

The absorbance of the sample at a certain wavelength can be calculated by comparing the detected light intensities

$$A = log\left(\frac{I}{I_0}\right), \quad (6)$$

where I is the intensity of light that passed through the sample and I_0 is the reference intensity.

From the Beer Lambert -law the absorption coefficient can be determined as

$$\alpha = \frac{ln(10)}{L}A, \quad (7)$$

where L is the thickness of the sample (in cm).

The absorption cross-section $\sigma(\lambda)$is determined by

$$\sigma(\lambda) = \frac{ln(10)}{NL}A, \quad (8)$$

where N is the RE -ion concentration (cm^{-3}). The RE -ion concentration can be estimated from the composition and density of the glass. [45, pp.11-15]

The absorption spectra were measured from polished samples using an UV-3600 Plus Shimadzu spectrometer with a resolution of 0.2 nm in the range 200-1700 nm.

3.5.2 Spectroscopic properties

Photoluminescence is the emission of light induced by an optical excitation of the sample. This emission of light occurs as radiative de-excitation occurs. Measuring emission at different wavelengths gives information of the population of the RE at different energy states.

A typical spectrofluorometer setup used to measuring luminescence is depicted in Figure 22.

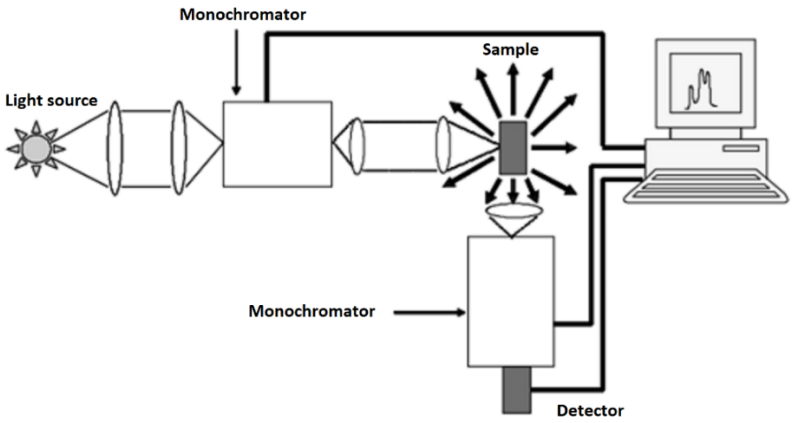

Figure 22. *Schematic diagram of a typical spectrofluorometer.* [45, p. 18]

A light source is aimed at the sample to excite the RE -ions in the glass to higher energy states. The emitted light from the sample is gathered by a collimating lens and a monochromator is used before reaching the detector to generate a spectrum.

The emission spectra in the ranges 1400-1700 nm and 450-750 nm were measured both from bulk glass and glass-ceramic samples as well as crushed powder samples. The powdered samples were placed in a sample holder to have similar volume between the measurements to allow the comparison of the intensity of the emission. The excitation was achieved using a 976 nm single-mode fiber pigtailed laser diode (CM962UF76P-10R, Oclaro). The gathered light emission was coupled to a waveguide and guided to a spectrometer (Instrument Systems Spectro 320). The emission spectra in the range 2550-2950 nm range was measured from crushed glass and glass-ceramic samples. The excitation was achieved using the same laser diode as for the other emission measurements. A monochromator coupled with an amplified MIR detector (detector PCI-4TE-4-1x1, preamplifier PIP-DC-200M-F-M4, Vigo) was used to acquire MIR emission spectra.

3.5.3 Judd-Ofelt theory

Judd-Ofelt theory enables the estimation of transition probabilities, radiative lifetimes and branching ratios of emission for lanthanide ions in solid matrices. The theory is extensive and therefore will not be discussed here in full detail, detailed description can be found in the works of Judd [50] and Ofelt [51].

Rare-earth ions exhibit sharp spectral lines. The sharp spectral lines are to be expected for the transition between states in the *4f* electronic shell. These transitions are however forbidden according to the Laporte selection rule, meaning that the transition probability

is expected to be low. The Laporte rule states that the sum of angular momenta of electrons in the initial and final state must change by an odd integer. The proposed mechanism for rare-earth ions in solids to exhibit these transitions is that a crystalline- or ligand field in solids could distort the electronic motion mitigating the selection rules considered for free atoms. Rare-earth ions in solid matrices are free-atom-like as the *4f* shell is shielded from outside influences by the screening of outer electron shells. The crystal- or ligand field allows the transitions between *4f* states resulting in sharp spectral lines. The transitions however have lower intensity than what would be expected for free atoms. Judd-Ofelt theory is capable of predicting intensities for the transitions. [52, pp. 403-411]

In the Judd-Ofelt theory, the line strength S_m is determined as

$$S_m = \frac{3ch(2J+1)}{8\pi^3 e^2 \bar{\lambda}} n \left(\frac{3}{n^2+2}\right)^2 \int_{band} \alpha(\lambda)\, d\lambda, \tag{9}$$

where c is the speed of light, h is the Planck's constant, n is the refractive index of the material, $\bar{\lambda}$ is the mean wavelength of the absorption peak, e is the electron charge and $\int_{band} \alpha(\lambda)\, d\lambda$ is the integrated area of the absorption cross-section of an absorption peak. The Judd-Ofelt parameters Ω_λ (λ = 2, 4, 6) can be determined by fitting the experimental expression (9) with the Judd-Ofelt expression for theoretical line strength

$$S_{ED}(J, J') = \Sigma_{\lambda=2,4,6} \Omega_\lambda \left|\langle J||U^{(\lambda)}||J'\rangle\right|^2, \tag{10}$$

where J' is the total angular momentum of the initial state, J is the total angular momentum of the final state for a transition. The $\langle||U^{(\lambda)}||\rangle$ are double reduced matrix elements of unit tensor operators which can be considered to be independent of host matrix.

The expression (10) can be by a presented equation set with N equations

$$S_j^t = \Sigma_{i=1}^3 M_{ij} \Omega_i, \tag{11}$$

where M_{ij} are components for the square matrix elements of $U^{(2)}$, $U^{(4)}$ and $U^{(6)}$. The Ω_i parameters correspond to Ω_λ (λ = 2, 4, 6). N represents number of transitions to be fit. As we have three Judd-Ofelt parameters, it is required that N must be equal to or greater than 3.

The sum of the squared difference is given by

$$\sigma^2 = \Sigma_{j=1}^N \left(S_j^m - \Sigma_{i=1}^3 M_{ij} \Omega_i\right)^2. \tag{12}$$

When the derivative with respect to Ω_k is set to zero, the sum of the squared difference can be minimized,

$$\frac{\partial(\sigma^2)}{\partial\Omega_i} = -2\Sigma_{j=1}^{N} M_{ji}\left(S_j^m - \Sigma_{i=1}^{3} M_{ij}\Omega_i\right) = 0. \tag{13}$$

Now the set of Judd-Ofelt parameters which minimizes the fitting can be solved. From equation (13) we get

$$\Sigma_{j=1}^{N} M_{ji} S_j^m = \Sigma_{j=1}^{N} M_{ji} \Sigma_{i=1}^{3} M_{ij}\Omega_i, \tag{14}$$

and by transposing the matrix we have $M_{ji} = M_{ij}^T$.

Now each parameter can be solved as

$$\Omega_i = (M^T M)^{-1} M^T S_m. \tag{15}$$

The Judd-Ofelt parameters can be used to estimate the electric dipole transition probability for transition $J \rightarrow J'$. This is given by the Einstein A coefficient as

$$A(J', J) = \frac{64\pi^4 e^2}{3h(2J\prime+1)\bar{\lambda}^3}\left[n\left(\frac{n^2+2}{3}\right)^2 S_{ED} + n^2 S_{MD}\right] = A_{ED} + A_{MD}, \tag{16}$$

where S_{ED} and S_{MD} are the electric and magnetic dipole strengths, respectively.

The electric dipole strength was given in equation (10) and the magnetic dipole strength is expressed by

$$S_{MD} = \frac{h^2}{16\pi^2 m^2 c^2}|\langle (S, L)J||L + 2S||(S', L')J'\rangle|^2, \tag{17}$$

where m is the electron mass, S is the spin and L is the angular momentum.

The matrix elements corresponding to magnetic dipole transitions are nonzero only if the following selection rules are considered: $\Delta S = 0$, $\Delta L = 0$, $\Delta J = 0, \pm 1$. Finally, the branching ratios are given by

$$\beta_{J'J} = \frac{A(J\prime, J)}{\sum_J A(J', J)}. \tag{18}$$

Judd-Ofelt theory can be further utilized to estimate lifetimes of the different states with an error less than 30 % compared to experimental values. [52, pp. 239-425]

3.6 X-ray diffraction analysis

X-ray diffraction (XRD) is an effective method to study the atomic arrangement and especially long-range order of crystalline structures. The technique is based on studying the intensity distribution formed by the interference of elastically scattered X-rays from crystalline structures. The obtained interference patterns are compared to an extensive database of studies to determine the crystal phases present in the sample. [53, pp. 2-3]

X-ray is a form of energetic electromagnetic radiation with a wavelength in the 0.01-100 Å range. Typically, in XRD, X-rays with a wavelength close to 1 Å are used as they are close to the distances between crystal planes. As X-rays hit the sample, some of the X-rays are elastically scattered maintaining the incident wavelength. The scattered rays form a diffraction pattern specific to the crystal. The diffraction pattern can be described by the Bragg law which states that diffraction peaks are perceived at an angle θ according to

$$n\lambda = 2d \sin\theta, \tag{19}$$

where d is the distance between adjacent crystal planes, λ is the wavelength of the incident X-ray beam, θ is the incident and the reflected angle and n is the order of reflection.

A long-range periodic structure is a requirement to see interference peaks. Various diffraction patterns are presented in Figure 23.

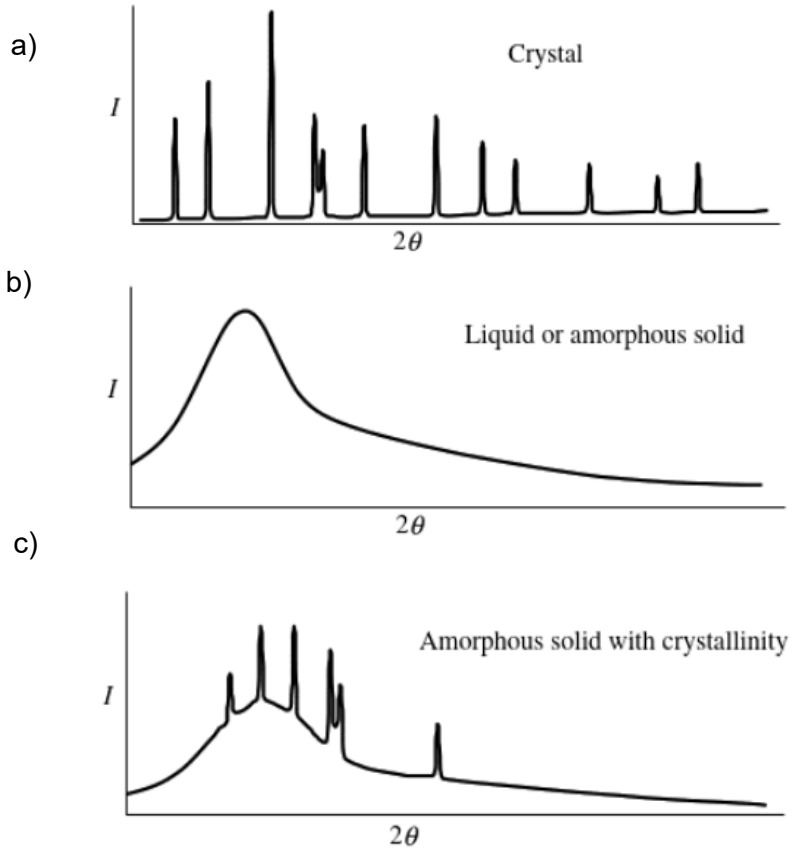

Figure 23. *Diffraction patterns from various materials a) crystal, b) liquid or amorphous solid, c) amorphous solid with crystallinity.* [53, p. 15]

As can be seen from Figure 23,

- **the diffraction pattern of a crystal** consists of sharp and distinct peaks corresponding to various crystal planes.
- **for amorphous materials** without long range order, no sharp peaks can be seen in the XRD pattern as the X-rays are not diffracted periodically and therefore no interference peaks are formed. Instead, a broad distribution with one or two peak values can be seen. The distribution of atomic distances in the material can be seen from the shape of band.
- **for amorphous materials containing crystalline parts**, the diffraction pattern has the background corresponding to the amorphous part and diffraction peaks from the crystals.

The XRD setup usually consists of an X-ray source, X-ray optics, and a detector. The detector and X-ray source are moved along a goniometer circle to detect the X-rays diffracted at different angles and gather a spectrum. A schematic of a typical XRD measurement setup is presented in Figure 24.

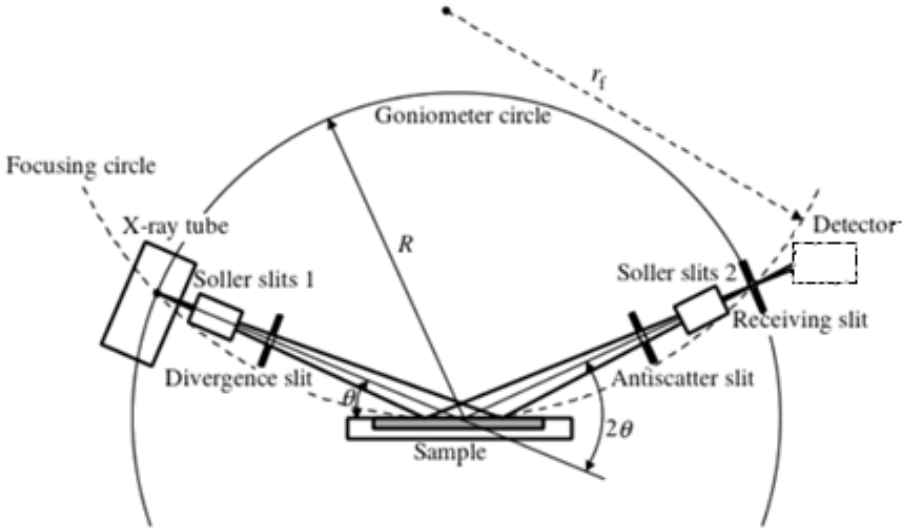

Figure 24. *Schematic diagram of an X-ray diffractometer. The main components are labeled. Adapted from [53, p. 60].*

An X-ray tube or a rotating anode generator is used as an X-ray source. Electrons that are emitted at the cathode are accelerated using a voltage. X-ray radiation is generated as electrons hit the anode. The X-ray spectrum depends on the used voltage as well as the anode material. The radiation consists of characteristic peaks and continuous radiation known as Bremsstrahlung. To get rid of the different X-ray wavelengths, a filter is used before the detector. The X-ray optics are needed to manipulate the X-ray beam to have a desired intensity, cross-section size and spectral purity. [53, pp. 52-60]

The XRD pattern of the investigated samples were measured by a Panalytical EMPYREAN multipurpose X-ray diffractometer using cobalt Kα radiation (λ = 1.5405980Å). The data were collected from 2Θ = 15°-60° in 0.026° intervals. The samples were crushed into a fine powder and analyzed using a zero background Si-plate to have no background from the sample holder.

3.7 X-ray photoelectron spectroscopy

X-ray photoelectron spectroscopy (XPS) is an analysis method used to analyze the elemental composition of the sample surface. XPS is based on the photoelectric effect, in which energetic photons can cause emission of electrons from the irradiated surface. If the energy of an incident photon overcomes the electron binding energy, an electron is emitted. The kinetic energy (E_k) of the electron is given as:

$$E_K = h\nu - E_B - \phi, \tag{20}$$

where E_B is the binding energy of the orbital from where the electron is ejected and ϕ is the work function of the spectrometer. The binding energy E_B equals to the energy difference of the initial atom and the ion.

These binding energies are element specific. In XPS, the kinetic energies of the ejected electrons are measured. As the other terms are known, the binding energies and thus the elemental composition can be deduced. [54, pp. 8-9]

The emission of an electron leaves a vacancy in the shell it was ejected from. This vacancy can be filled from another energy level, the excited state can then be de-excited by the emission of another electron, this process is known as Auger electron emission. A common notation used is to state first the shell from which the initial electron was ejected from, then the shell where the vacancy is filled from and finally the shell from which the Auger electron is ejected from. For example, *KLL* emission would be the case, where the initial electron is ejected from the *K* level, the hole is filled by an electron from some *L* level and an Auger electron is emitted from some *L* level. [48, pp. 8-9]

The binding energies are slightly affected by the chemical environment of the photoemitting atom. Variations in the bond distance with neighboring ions/atoms and oxidation state of the photoemitting atom among others cause a shift in the position of the gathered peaks. The analysis of these shifts gives additional information of the environment of the photoemitting atoms. Additionally, the peak intensity gives quantitative information of the photoemitting specimen. [54, pp. 25-26]

The main part of an XPS setup consists of a vacuum chamber, an X-ray gun, a hemispherical analyzer (CHA) and a detecting system. In addition, the setup contains instrumentation to achieve and maintain the vacuum as well as instrumentation to introduce the sample to the analysis chamber.

A typical XPS setup is depicted in Figure 25.

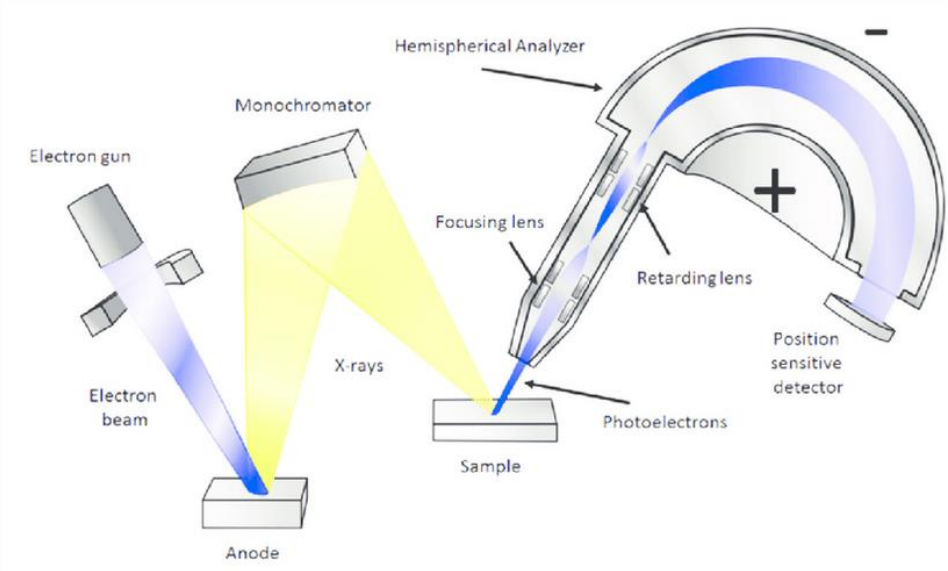

Figure 25. *A schematic picture of a typical XPS setup*. [55]

The XPS experiments are done in vacuum to enable the ejected electrons not to lose their energy before reaching the detector. Additionally, vacuum makes it possible to avoid the formation of contaminant and adsorbent layer on the sample surface. An X-ray gun is used to generate suitable energy photons for surface analysis. Often Mg Kα and Al Kα are used due to their various properties such as minimal energy spread, high intensity and good heat conductivity. The measurement of the electrons kinetic energy utilizes a hemispherical analyzer. The ejected electrons go through an electron lens which retards the electrons to a suitable energy. The potential difference between the spheres of the hemispherical analyzer determines the energy range of which electrons can pass along the radius. Electrons with different energies reach different spots on the detector and the kinetic energy can be determined. The potential of the electron lens is varied so that different energy electrons pass the lens and a spectrum is gathered. [54, pp. 27-46]

XPS is a surface sensitive analysis method. Only the electrons that reach the detector without losing energy contribute to the spectral peaks. Electrons that lose kinetic energy due to interactions such as inelastic collisions contribute to the spectral background. As the cross-section of electron interaction with matter is high, only electrons from near the surface contribute to the peak signals. The distance an electron with a given energy propagates in a given material without losing some of its energy is known as inelastic mean free path (IMFP). By tuning the energy of incident light, the IMFP can be tuned. The surface sensitivity of XPS enables its use in analyzing the composition of thin films,

the signal is gathered from the thin films instead of from the substrate. Signal can be gathered from the outer ~10 nm layer. [54, pp.9-12]

The XPS spectra of the deposited thin films were measured using the setup described in detail by Lahtonen et al. [56]. An Al Kα irradiation source was used with a 0° tilting angle of the sample. This measurement was performed in collaboration with Prof. Mika Valden and his group.

4. RESULTS AND DISCUSSION

The aim of this study was to prepare and characterize glasses and glass-ceramics in order to prepare glass-based materials with strong emission at 2.7 µm which could be deposited into films. For this purpose, the choice of rare-earth was Er^{3+} ions due to the $^4I_{11/2} \rightarrow {}^4I_{13/2}$ (2.7 µm) transition. Germanate glasses were chosen due to their low phonon energies and high IR transmission. Different network modifiers and intermediates were introduced to this glass system to find a suitable composition for good emission properties of the RE.

In this thesis, we first explain the impact of the glass composition on their thermal and optical properties. Then we discuss the impact of the crystals formation in the glass on the spectroscopic properties of the glasses. Finally, we present the preliminary results related to the film deposition.

4.1 MIR glass-based materials development and characterization

4.1.1 Impact of glass composition on the structural and optical properties of the glasses

Glasses of the molar composition $64GeO_2$-$9.9Ga_2O_3$-$11.3BaO$-$8.9Na_2O$-$1Er_2O_3$-5MO with MO = Al_2O_3, TiO_2, Y_2O_3 and ZnO in mol% were prepared using the standard melting process in air as described in section 3.1. The densities and thermal properties of the glasses are presented in Table 2.

Table 2. *Densities and thermal properties of 1Er glasses.*

Sample	ρ ± 0.02 g/cm^3	T_g ± 3°C	T_x ± 3°C	T_p ± 3°C	ΔT (T_x-T_g) ± 6°C
1ErAl	4.16	610	783	835	190
1ErTi	4.28	588	792	848	204
1ErY	4.40	626	846	910	227
1ErZn	4.35	563	782	863	219

The density follows the increasing molar mass of the elements in the order Al < Ti < Zn < Y. The presented thermal properties were determined from the DTA curves in Figure 26 as described in section 3.3.

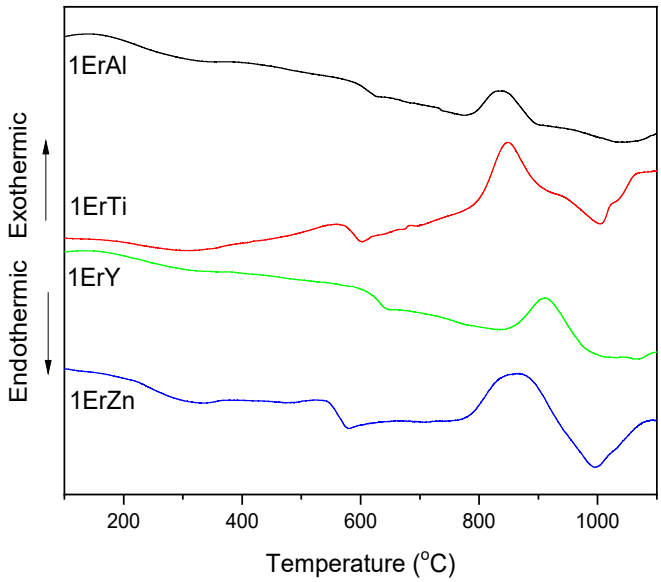

Figure 26. *Thermogram of the glasses.*

Determining the thermal properties is of importance to determine the temperatures for heat treatment for the controlled nucleation and growth of crystals.

- The 1ErY glass has the highest T_g which indicates a stronger glass network than the other glasses.
- The 1ErZn glass has the lowest T_g, correspondingly indicating the weakest network among the glasses.

$\Delta T = T_x - T_g$ is used to evaluate the thermal stability of the glass against crystallization. A glass is considered thermally stable if ΔT is near or above 90°C. All of the prepared glasses have great thermal stability and so are good candidates to be deposited into films. No crystallization is expected to occur during the film deposition.

The normalized Raman spectra of undoped glasses are presented in Figure 24. The 0Er glasses were melted only for the purpose of using them in this measurement to avoid a strong background signal from the luminescence of Er^{3+} ions.

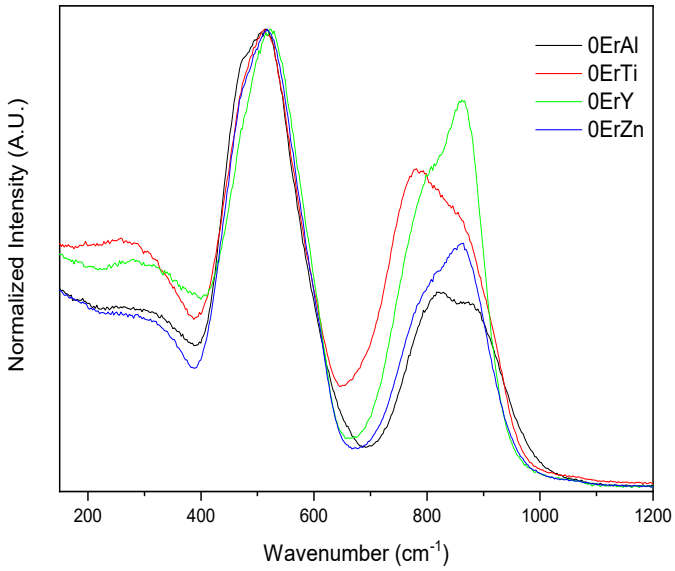

Figure 27. *Raman spectra of the undoped glasses.*

The spectra are normalized to the maximum intensity band, therefore all the intensity changes are relative to the main peak. The spectra exhibit bands at 200-400 cm^{-1}, a main band with the maximum at ~500 cm^{-1} and a band at 700-1000 cm^{-1}.

The band at 200-400 cm^{-1} is assigned to the network modifying cation vibrations in large interstitial sites. The two bands at 250 and 370 cm^{-1}, can be attributed to the Raman active bending modes of Q^2 and Q^1 tetrahedra. The main band consists of at least two sub-bands with maxima at about 465 and 520 cm^{-1}. These bands are contributed to the four- and three-membered GeO_4-ring structures, respectively. [57]

The high frequency band at 700-1000 cm^{-1} consists of at least two sub-bands with maxima at 860-890 and 780-820 cm^{-1}. Raman vibrational bands in the high frequency range are associated with GeO_4 tetrahedra having *n* bridging oxygens (*n*=4, 3, 2, 1 or 0). It is known that the depolymerization of GeO_2 glass increases the number of non-bridging oxygens in the glass and Q^4- units transform to Q^3, Q^2, Q^1 and Q^0 units with typical Raman frequencies of 865, 780, 740 and 720 cm^{-1}, respectively, while the whole Q-species “envelope” shifts to the lower frequencies [57] At the same time, less membered rings are membered and GeO_4-rings start to dominate, resulting in a change of the ratio between the bands at 465 and 520 cm^{-1} as the relative contribution of the latter band is higher upon depolymerization. [57] [58].

The highest number of 4-membered rings as well as significantly higher vibrational frequencies of the Q-species range vibrational bands are observed for the Al containing glass, allowing to conclude that introduction of aluminium results in formation of the most polymerized glass network. Aluminium is commonly considered as an intermediate in glasses. However, 5- and 6-fold coordinated Al-species are known to play the role of modifiers. Often these species are formed in the case of a deficiency of modifiers in the glass to stabilize AlO_4-tetrahedra in the network. The glass composition under investigation contains excessive number of modifiers and the formation of highly coordinated alumina species is hardly possible. At the same time presence of AlO_4-tetrahedra in the glass requires their charge compensation and part of the cations present in the glass (Ba^{2+} or Na^{+}) are used for this upon introduction of Al_2O_3 in the glass. This results in the decrease in the number of non-bridging oxygen and more a polymerized glass network. [14]

Raman spectra observed for the Zn containing and Y containing glasses are similar. For both, the contribution at 465 cm^{-1} is significantly lower as compared to Al containing glass. At the same time the positions of the high frequency bands at ~860 and 790 cm^{-1} evidence the presence of Q^3 and Q^2 species in these glasses, respectively. Among the two glasses, the Y containing glass has higher relative intensity of the 520 cm^{-1} vibrational band as well as higher intensity of the Q-species envelope, meaning that this glass is more depolymerized than the Zn containing glass. This is explained by the difference in the formal valency state between Zn^{2+} and Y^{3+} ions as well as a higher number of Y-ions introduced, since doping with 5 mol % of Y_2O_3 corresponds to 10 mol % of $YO_{2/3}$ (compared to 5 mol % of ZnO). Both the elements play a role of network modifier in the glass.

The titanium containing glass demonstrates a somewhat mixed behavior: the relative intensity of the 460 cm^{-1} band is slightly higher than in the Y containing and Zn containing glasses, and lower than in the Al containing glass, i.e. the polymerization of the Ti containing glass should also be in between. At the same time, the Q-species envelope is at significantly lower frequencies, with the most intense band at ~780 cm^{-1}. This could be interpreted as formation of Q^2 species and significant depolymerization of the glass. However, it is well known that titania can form TiO_4-tetrahedra in the glasses, which have Raman active modes at about 750 cm^{-1} [59]. Therefore, the observed inconsistency in the Raman spectra of the Ti containing glass can be explained by overlapping of Germanium Q-species band with Ti-O vibrational band due to the presence of TiO_4 tetrahedra.

It is known that upon introduction of a network modifier germanate glasses demonstrate an extremum of their macroscopic properties at a specific amount of the modifier. For instance the density maximum for binary xNa_2O-$(1-x)GeO_2$ glasses is observed at x=15 [60]. The exact value of the modifier to have this extremum depends on the used element [59]. It may be assumed that among the investigated glasses, the Y containing glass has the closest composition to the extremum of in the glass properties and that this glass possesses the most packed glass network, due to a higher number of 3-membered GeO_4-rings. This would also explain the higher T_g compared to other investigated glasses (Table 2).

The FT-IR spectra of the 1Er glasses are presented in Figure 28. The spectra were gathered using the ATR mode.

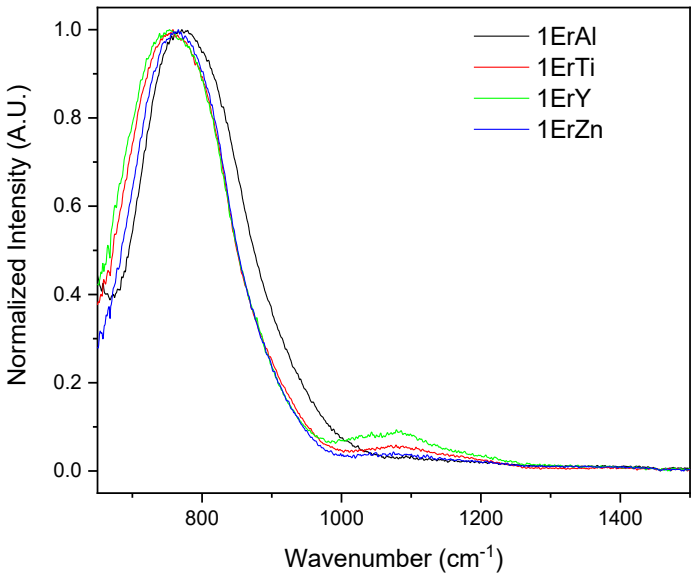

Figure 28. *FTIR spectra of the glasses.*

The spectra show a broad band spanning in the 700-900 cm^{-1} range. The band comprises of various overlapping bands. [61] The spectra show a slight shift of this band to lower wavenumbers: 1ErAl and 1ErY demonstrate the highest and the lowest vibrational frequency of this band respectively. The low frequency part of this peak could be associated to v_{as}(Ge-NBO) vibrations in Q^3 species (typical position is 780-793 cm^{-1}), whereas higher frequency shoulder is associated with to v_{as}(Ge-O-Ge) vibrational mode of Ge-O-Ge bridges [57]. Thus, the shift of this band could be considered as an evidence of the depolymerization degree of the glass, and Y containing and Al containing glasses are the most depolymerized and the most polymerized glass compositions respectively,

which is in agreement with the Raman spectra. The band at ~1100 cm^{-1} is often attributed to a X-O-Ge linkage bond, where X is a cation [62]. The increase in intensity of the band at ~1100 cm^{-1} in the spectrum of the 1ErY and 1ErTi samples might indicate that Y and Ti also participate in forming the glass network.

The IR transmittance spectrum of the glasses is presented in Figure 29.

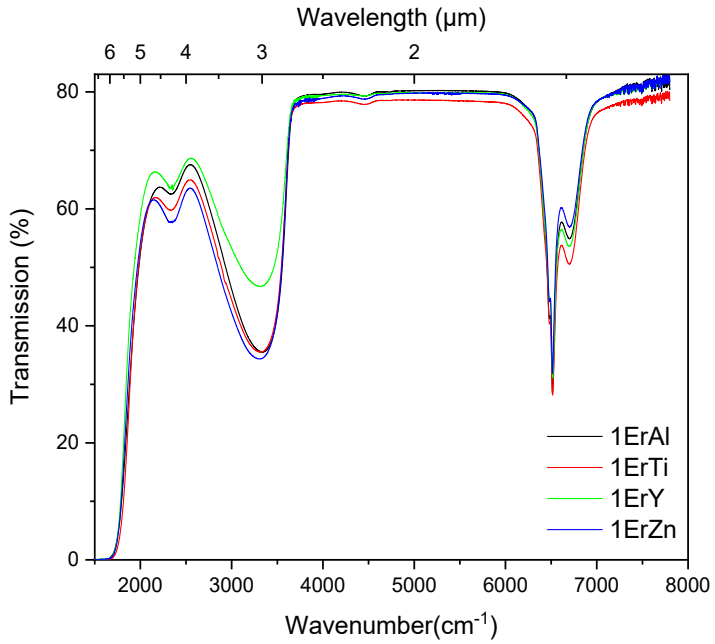

Figure 29. *IR transmittance spectra of the glasses with a thickness of about 3.2 mm.*

The spectra show about 78% transparency. The glasses have a wide transparency window with the IR cutoff edge being at around 5.4 μm confirming that the glasses are good candidates for applications at 2.7 μm. The spectra show three absorption bands.

- The absorption at around 6500 cm^{-1} (about 1.5μm) corresponds to the *4f-4f* transition of Er^{3+}-ions from the ground state $^4I_{15/2}$ to $^4I_{13/2}$ [6].
- The band at ~2300 cm^{-1} is attributed to the OH stretching vibration of very strongly hydrogen-bonded OH groups [63]
- The band at 2800-3500 cm^{-1} can be related to the “free” OH groups (weakly associated), the shoulder at 2800cm^{-1} being associated to OH “strongly associated” [63].

The OH absorption coefficient was calculated from the transmittance spectrum using the equation

$$\propto_{OH} = \frac{1}{L} \ln \frac{1}{T}, \tag{21}$$

where L is the sample thickness and T is the transmission at the peak of the OH band [63].

The spectra were then baseline corrected to determine the OH absorption coefficient. The OH absorption coefficient of the glasses is presented in Figure 30.

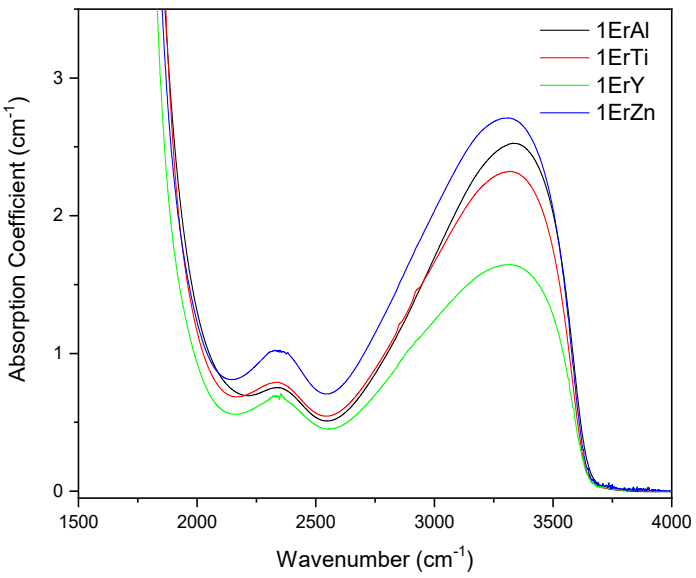

Figure 30. *The absorption spectra of the glasses.*

The OH absorption coefficient is dependent on the OH concentration in the glass: the higher the absorption coefficient, the larger amount of OH groups in the glass. The 1ErY glass has the lowest OH content. As the glasses were prepared with the same melting procedure, it is possible that the lower OH content can be related to the most packed glass network (due to the higher number of 3-membered GeO_4-rings). This tightly packed network leaves less “free” space within the glass network for the free OH to reside in. The 1ErZn glass with the least polymerized network has the highest OH content. The OH content is of importance as the energy transfer process from Er^{3+} to OH can greatly reduce the 2.7 µm emission.

The UV-VIS-NIR absorption spectra of the glasses are presented in Figure 31.

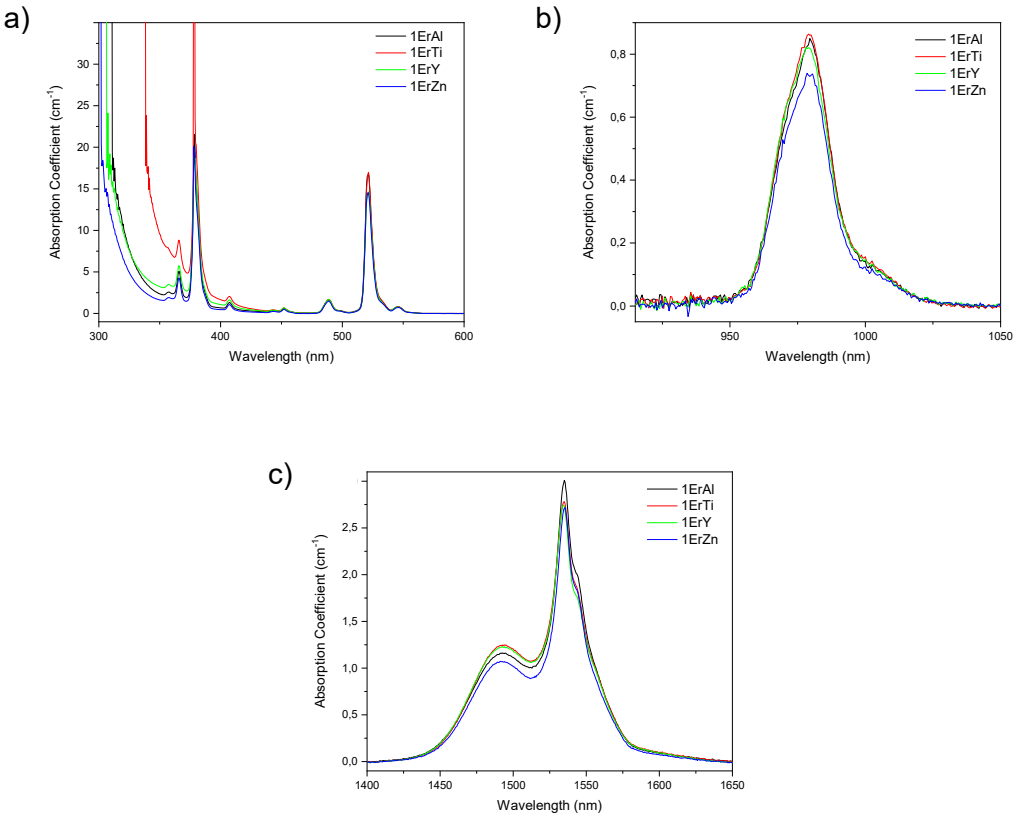

Figure 31. *The absorption spectra of the glasses (a) and the absorption bands centered at 980 nm (b) and 1530 nm (c).*

The absorption spectra presented in Figure 31 a) show the typical transitions of Er^{3+} ions from the ground state $^4I_{15/2}$ to various excited states. One can notice that the Ti containing glass has the UV absorption edge at higher wavelength compared to the other glasses most due to the presence of Ti^{3+} ions [64]. The other glasses show only small variation in the UV absorption edge position when changing the glass composition.

The absorption coefficients were determined from Figure 31 b) and c) and they were used to determine the absorption cross-sections at 980 nm and 1530 nm using equation (8). The Er^{3+} ion concentration was calculated from the density of the glass using the erbium molar percentage in the glass composition. The results are presented in Table 3.

Table 3. *The absorption coefficients and cross-sections of the glasses.*

Sample	Abs. coeff. at 980 nm /cm^{-1}	Abs. coeff. at 1530 nm/cm^{-1}	Er^{3+}(10^{20}) /ions/cm^3 ± 5%	σ_{Abs} at 980 nm (10^{-21}) /cm^2 ± 10%	σ_{Abs} at 1530 nm (10^{-21}) /cm^2 ± 10%
1ErAl	0.846	3.010	4.27	1.98	7.05
1ErTi	0.863	2.781	4.43	1.95	6.27
1ErY	0.821	2.745	4.29	1.91	6.40
1ErZn	0.737	2.716	4.50	1.64	6.03

The absorption cross-section is changed depending of the additional element introduced in the glass, indicating that changes in the glass network influence the Er^{3+} ions local environment (site) in the investigated glasses. For comparison, absorption cross-sections of various erbium doped glasses are presented in Table 4.

Table 4. *Absorption cross-sections of various glasses.*

Glass	σ_{Abs} at 980 nm (10^{-21}) /cm^2	σ_{Abs} at 1530 nm (10^{-21}) /cm^2	Reference
Silicate ED2	1.31	-	[65]
Phosphate L12	2.01	-	[65]
Phosphate L28	2.47	-	[65]
Fluorophosphate L11	2.46	-	[65]
Fluorophosphate L14	2.15	-	[65]
Fluorozirconate ZBLAN	1.15	-	[65]
Zinc tellurite (73.3TeO_2-19.6ZnO-4.9Na_2O-1.1La_2O_3-1.1Er_2O_3)	3.45	-	[66]

Germanate ($65GeO_2$-$12Ga_2O_3$-23(BaF_2-La_2O3-Li_2CO_3-Er_2O_3))	2.2	6.0	[67]

The absorption cross-sections at 980 nm of the prepared glasses are similar to that of the $65GeO_2$-$12Ga_2O_3$-23(BaF_2-La_2O3-Li_2CO_3-Er_2O_3) glass shown in Table 4. One can notice that they are higher than that of silicate and Fluorozirconate glasses but comparable to those measured in phosphate and fluorophosphate glasses. The prepared glasses had a lower absorption cross-section compared to a zinc tellurite glass.

From the absorption spectra, the Judd-Ofelt parameters were calculated according to Judd-Ofelt theory presented in chapter 2.4. The refractive index of the glasses needed for the calculation was taken to be equal to n=1.7 for all glass compositions, based on previous study on a similar glass system and the squared matrix elements $||U^{(\lambda)}||^2$ were given by Carnall et al [68]. The δ_{rms} values were determined as root-mean-square error deviation between the determined experimental and calculated oscillator strengths. The JO parameters are presented in Table 5.

Table 5. *The Judd-Ofelt parameters of the prepared glasses.*

Sample	Ω_2**(10^{-20} cm^2)**	Ω_4**(10^{-20} cm^2)**	Ω_6**(10^{-20} cm^2)**	δ_{rms}**(10^{-6})**
1ErAl	7.60	1.14	1.31	0.50
1ErTi	7.28	1.20	1.30	0.52
1ErY	6.64	1.23	1.35	0.54
1ErZn	6.26	1.01	1.16	0.47

The small δ_{rms} values indicate the validity of the theory as well as reliability of the calculations. The Judd-Ofelt parameters give information about the local structure and bonding in proximity to the rare-earth ions [69]:

- the Ω_2 parameter is related to the covalency of the RE-ligand, the polarizability of the ligand anions and the coordination symmetry of the RE -ion environment.
- the Ω_4 and Ω_6 parameters give information about the long-range effect of the glass host such as viscosity, density and rigidity.

For comparison, the Judd-Ofelt parameters of various Er^{3+} doped glasses are presented in Table 6.

Table 6. *Judd-Ofelt parameters in various Er^{3+} doped glasses.* [70]

Sample	Ω_2**(10^{-20} cm^2)**	Ω_4**(10^{-20} cm^2)**	Ω_6**(10^{-20} cm^2)**
Aluminate	5.60	1.60	0.61
Germanate ($55GeO_2$-25(BaO+ZnO+K_2O)-15PbO-5PbF_2-1Er_2O_3)	5.15	1.36	0.59
Germanate ($57GeO_2$-26.1K_2O-16.5BaO-1Er_2O_3)	5.81	0.85	0.28
Silicate	4.23	1.04	0.61
Fluorophosphate	2.91	1.63	1.26
Fluoride	2.91	1.27	1.11

The Ω_2 parameter of the investigated glasses is larger than those reported in other glass hosts suggesting that the Er-ligand bonding is covalent, the polarizability of the ligand anions and/or the coordination symmetry of the RE -ion environment high. Of the prepared glasses, the Ω_2 is largest for the 1ErAl glass and lowest for the 1ErZn glass.

The Ω_6 of the prepared glasses is high compared to other glass systems, especially the germanate glasses presented in Table 5, suggesting large rigidity of the investigated glasses. Of the prepared samples the 1ErY glass has the highest Ω_4 and Ω_6 values, indicating that it has the highest rigidity of the glasses. This is in agreement with the structural analysis. Respectively, the 1ErZn glass has the lowest Ω_4 and Ω_6 values, indicating that it has the lowest rigidity of the glasses. This is in agreement with it having the lowest glass transition temperature, i.e. weakest most depolymerized glass network.

The magnetic dipole spontaneous emission probability A_{md} was calculated using the A_{md} values for Er^{3+} in LaF_3 [65] and corrected for the refractive index:

$$A_{md} = \left(\frac{n}{n'}\right)^3 A_{md}'. \quad (22)$$

Finally, the branching ratios for different transitions were calculated and are presented in Appendix A.

The branching ratio values for the transitions $^4I_{13/2} \rightarrow {}^4I_{15/2}$, $^4S_{3/2} \rightarrow {}^4I_{15/2}$, and $^4F_{9/2} \rightarrow {}^4I_{15/2}$ are 1, 0.67 and 0.88-0.89, respectively, confirming the possibility for achieving efficient IR, green, red emissions under suitable excitation [71].

The emission spectra upon 976 nm excitation is presented in Figure 32.

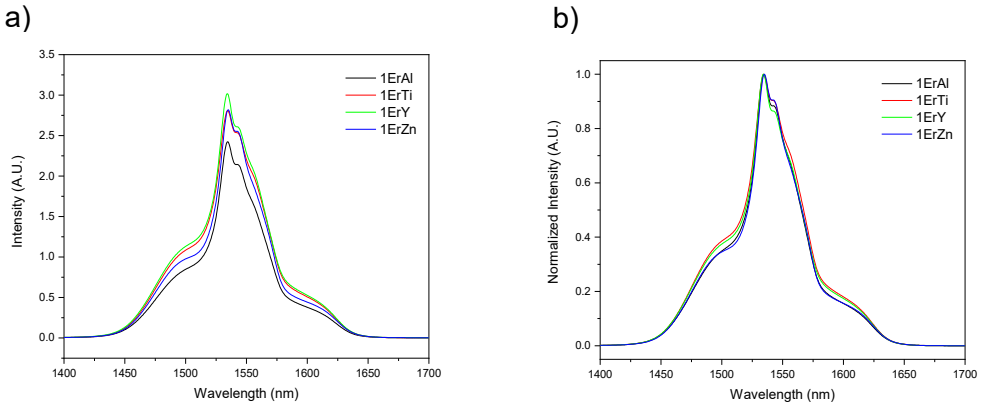

Figure 32. *The emission spectra of the investigated glasses under 976 nm excitation with a) intensity and b) normalized intensity.*

The emission spectra exhibit a similar broad band which is typical of the emission of Er^{3+} ions in amorphous network confirming that despite some changes in the local environment the Er^{3+} ions are still located in similar sites in the glasses. According to McCumber theory the emission and absorption cross-sections are related with each other as:

$$\sigma_{abs} = \sigma_{em} \exp\left(\frac{h\nu - E_0}{k_B T}\right)$$

This implies, that the emission intensity should follow the same trend as the absorption, which is however not the case and the highest intensity of the emission was recorded from the 1ErY glass. Therefore one more factor should influence the luminescence intensity. This behavior can be explained by lower OH content in 1ErY glass in comparison to other glasses as evidenced from IR absorption measurement (Figure 30).

The up-conversion emission spectra upon 976 nm excitation is presented in Figure 33.

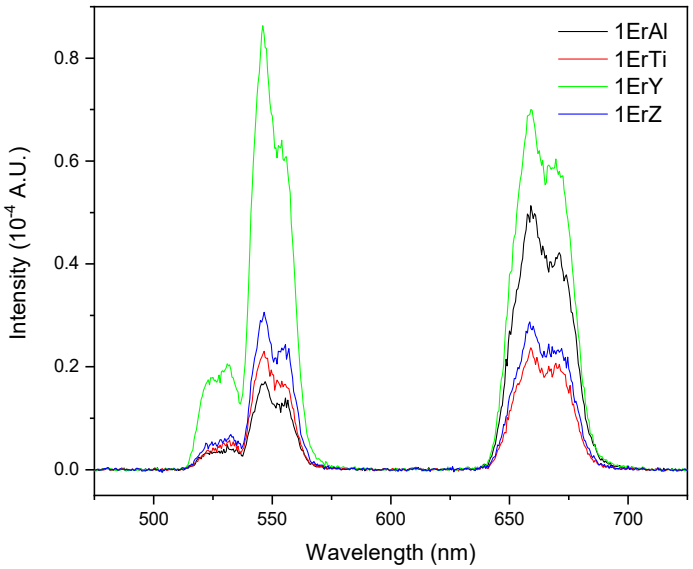

Figure 33. *The up-conversion emission spectra of the investigated glasses under 976 nm excitation.*

As seen in Figure 33, the spectra exhibit emission bands at around 520 nm, 550 nm and 660 nm. The band at 660 nm is attributed to the $^4F_{9/2} \rightarrow {}^4I_{15/2}$ transition, the 520 nm band to the $^2H_{11/2} \rightarrow {}^4I_{15/2}$ transition and the 550 nm band to the $^4S_{3/2} \rightarrow {}^4I_{15/2}$ transition. The Er^{3+} ions can populate the $^4F_{7/2}$ by excited state absorption from the $^4I_{11/2}$ level or by an energy transfer up-conversion process when an excited Er^{3+} ion in the $^4I_{11/2}$ state transfers its energy another Er^{3+} ion also in the $^4I_{11/2}$ state. The $^4F_{7/2}$ state can then decay to the levels $^2H_{11/2}$, $^4S_{3/2}$ and $^4F_{9/2}$ through non-radiative relaxation processes. The $^4F_{9/2}$ state can also be populated through excited state absorption from $^4I_{13/2}$ or an energy transfer up-conversion process: $^4I_{11/2} + {}^4I_{13/2} \rightarrow {}^4F_{9/2} + {}^4I_{15/2}$. [6] [72] The measured up-conversion emission intensity was low compared to the emission intensity at 1530 nm. The 1ErY glass exhibits high intensity of green and red emissions compared to the other glasses.

The MIR emission spectra upon 976 nm excitation was measured, but no signal could be detected probably due to the large OH content in the glass and also the low Er_2O_3 content. Therefore, new glasses were prepared with 2.5 mol% Er_2O_3. The thermograms of the glasses are presented in Figure 34.

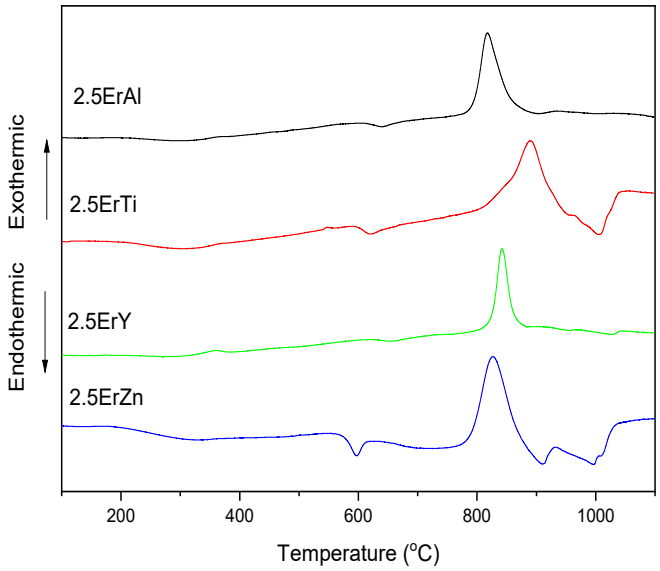

Figure 34. *The DTA curves of the 2.5Er glasses.*

The thermal properties were determined from Figure 34. The determined densities and thermal properties are presented in Table 7.

Table 7. *Densities and thermal properties of the 2.5Er glasses.*

Sample	ρ ± 0.02 g/cm^3	T_g ± 3°C	T_x ± 3°C	T_p ± 3°C	ΔT (T_x-T_g) ± 6°C
2.5ErAl	4.30	630	790	816	160
2.5ErTi	4.43	609	800	892	191
2.5ErY	4.55	642	821	842	179
2.5ErZn	4.46	588	786	827	198

The 2.5Er samples show similar trends in glass transition temperature and density depending on the glass composition as the previous glass series. However, the glass transition temperature increases by about 20°C for all the samples compared to the 1Er glasses. It was suggested that this effect could be due to the strong bonding and stabilization of non-bridging oxygens by highly coordinated Er ions [73]. A slight increase in density is also evident in all the samples compared to the 1Er glasses due to the addition of the heavy erbium replacing other elements in the glass.

All glasses exhibit emission centered at 2.7 µm under 976 nm excitation as shown in Figure 35.

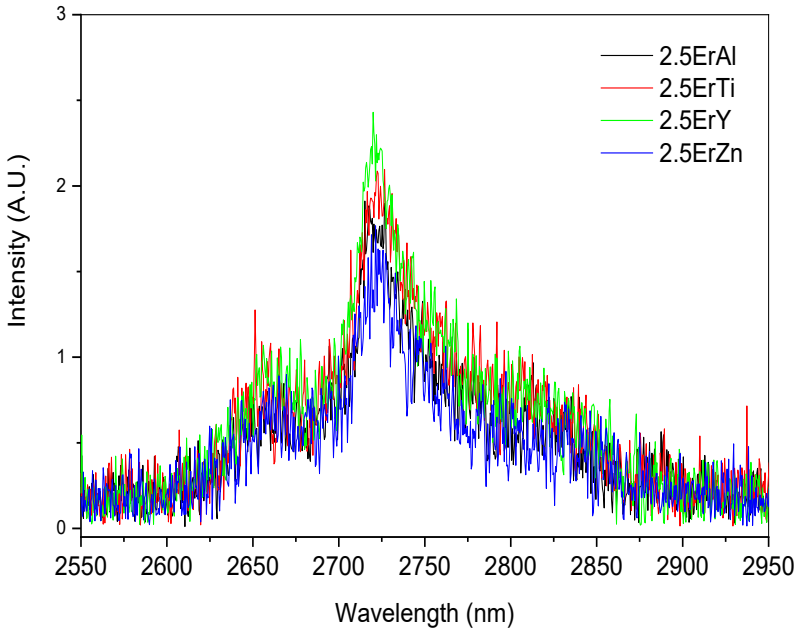

Figure 35. *The MIR emission spectra of the 2.5Er glasses under 976 nm excitation.*

One can notice that the order of increasing intensity aligns with the decrease in the OH content determined from IR absorption spectra (see Figure 30): the highest intensity of emission is seen for the 2.5ErY glass which is expected to have the lowest OH amount whereas the lowest intensity of emission is observed from the 2.5ErZn glass with highest OH amount. The results highlight the effect of OH groups in increasing the non-radiative relaxation of the $^4I_{13/2} \rightarrow {}^4I_{15/2}$ transition and therefore reducing the radiative emission at 2.7 µm. Nonetheless, the newly developed glasses are promising materials for MIR emission. Future effort should be focused on OH reduction in order to increase the intensity of the MIR emission.

4.1.2 Impact of crystallization on various glass properties

The 1Er and 2.5Er glasses were heat treated at T_g + 20°C for 17 h to form nuclei and at T_p for either 1 h or 6 h to grow the nuclei into crystals. The heat treatment times and temperatures are based on previous research [74] [75]. The 1Er and 2.5Er glasses seemed to behave similarly upon crystallization. A picture of the 2.5Er glasses before and after the heat treatments was chosen as an example and is presented in Figure 36.

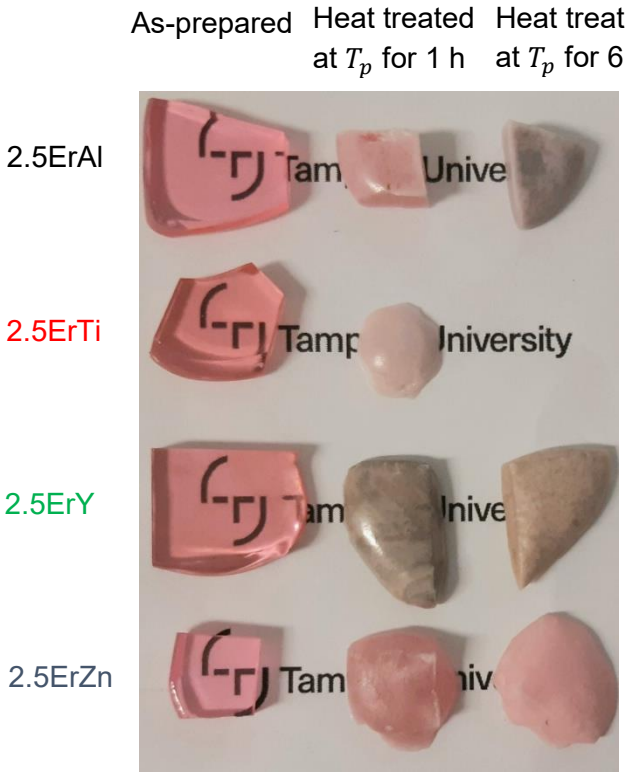

Figure 36. *Picture of the 2.5Er glasses before and after heat treatment.*

After heat treatment, all the 1Er and 2.5Er glasses have a ceramic appearance at the surface. This shows that crystallization occurs in all the glasses upon heat treatment. The inner part of the glasses has a glassy appearance confirming that the glasses exhibit surface crystallization.

As mentioned before, the 1Er glasses and 2.5Er glasses appeared to behave similarly upon crystallization, therefore only the 1Er glass-ceramics (GCs) were studied in more detail. The XRD patterns of the heat treated 1Er glasses are shown in Figure 37.

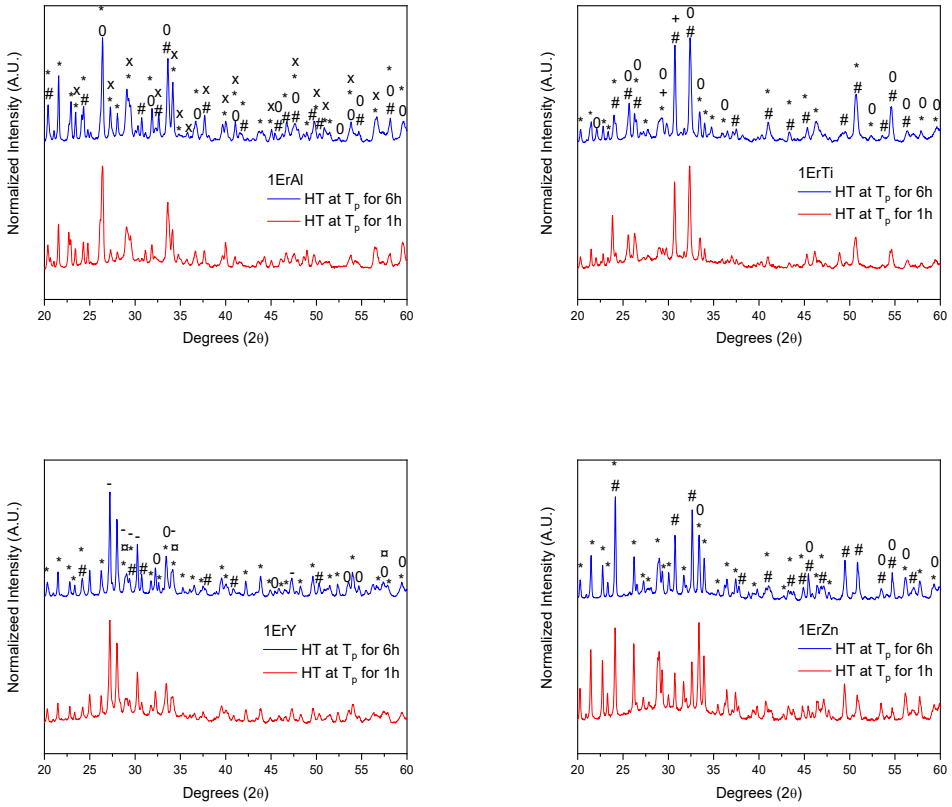

Figure 37. *XRD patterns of the heat treated 1Er glasses 1ErAl a), 1ErTi b), 1ErY c) and 1ErZn d).*

The symbols used for different crystals are presented in Table 8.

Table 8. *Symbols for crystals.*

Symbol	-	¤	+	x	0	*	#
Crystal	$Y_2[Ge_2O_7]$	Y_2O_3	$Er_2Ti_2O_7$	Al_2GeO_5	Ga_2O_3	$BaGa_2(GeO_4)_2$	$BaGe_4O_9$

For all of the samples, the 6 h heat treated glasses are more crystalline as the peaks are sharper than that of the corresponding 1 h heat treated samples. The XRD patterns of 1 h heat treated samples still contain low intensity broad band originating from the glass phase evidencing partial crystallization occurring during heat treatment for 1h. As seen from the XRD patterns, all of the glasses have multiple crystals precipitating during the heat treatment, the composition of which depends on the glass composition. Erbium containing crystals could be identified only in the 1ErTi glass.

The emission spectra at 1.5 μm of the GCs samples was measured under 976 nm excitation. The spectra are presented in Figure 38. It is clearly shown that

- the intensity of the emission from the 1ErAl, 1ErTi and 1ErZn glasses decreases after heat treatment while no significant changes in the intensity of the emission can be seen from the 1ErY glass. The decrease in the intensity of the emission can probably be related to changes in distances between the RE -ions. If the distances between the RE decrease, the interaction between RE is increased resulting in luminescence quenching. It is possible that the Er^{3+} ions that are not incorporated in the crystals are forced into a smaller volume leading to clustering leading to a decrease in the intensity of the emission.
- the heat treatment has no impact on the shape of the emission for the 1ErAl, 1ErTi and 1ErZn glasses indicating that the site of the Er^{3+} ions remain mostly unchanged after heat treatment. The shape of the emission band at 1.5 μm is not particularly sensitive to the site of Er^{3+}. So, the fact that the shape of emission does not change for the mentioned glasses, does not mean that the site of Er^{3+} is not affected at all. Sharp peaks can be seen in the emission band of the 1ErY glass suggesting that some Er^{3+} ions are located in crystals and/or the number of Er^{3+} ions sites is decreased after heat treatment.

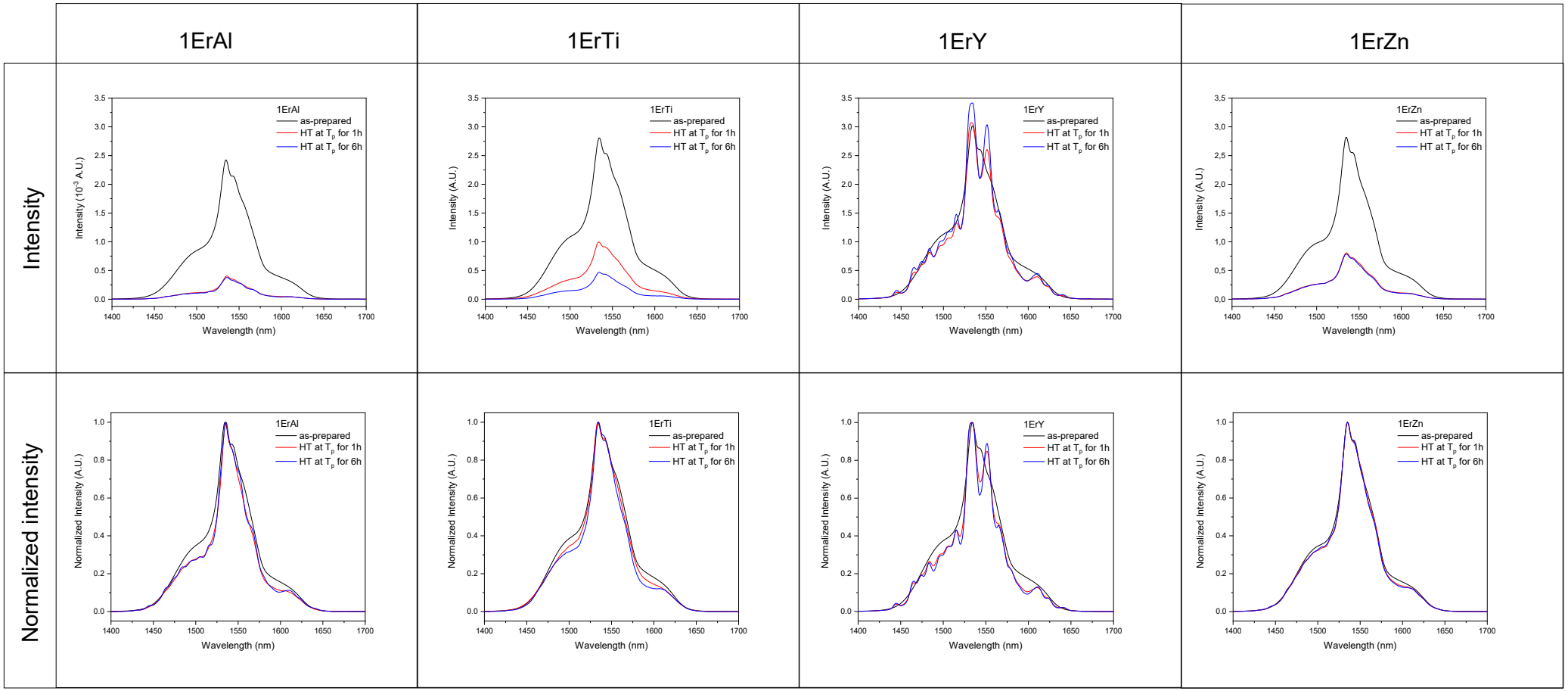

Figure 38. *Intensity and normalized intensity of the emission band at 1.5 μm under 976 nm excitation.*

As the glasses are suspected to exhibit surface crystallization, the emission spectra were collected both from the surface of bulk samples and from crushed powder samples. The powder samples are a mixture of the crystalline and amorphous phases. The emission spectra under 976 nm excitation are presented in Figure 39. Minor changes in the shape of emission between the surface of the bulk glass and from powdered sample can be seen suggesting that the Er^{3+} ions remain mostly in the amorphous network in the 1ErAl, 1ErTi and 1ErZn glasses. As for the 1ErY glass, as the intensity of the emission remains the same after heat treatment, the fact that the shape of the emission is the same when measured from the surface and from the powder might indicate that the heat treatment also leads to some bulk crystallization. This should be further investigated.

The up-conversion spectra of the glasses prior to and after heat treatment were measured from the powdered samples and are presented in Figure 40. The heat treatment leads to a significant increase in the intensity of the up-conversion probably due to the decrease in the Er-Er distances. The increase in emission intensity is the strongest in the 1ErY sample and smallest in the 1ErAl sample. One can also notice changes in the shape of the emission bands is different after heat treatment indicating that the site of Er^{3+} is indeed somewhat modified after heat treatment. Changes in the shape of the up-conversion emission bands are more prominent than that of the 1.5 μm emission band because the transitions related to the up-conversion emissions are more sensitive to the local environment of Er^{3+}.

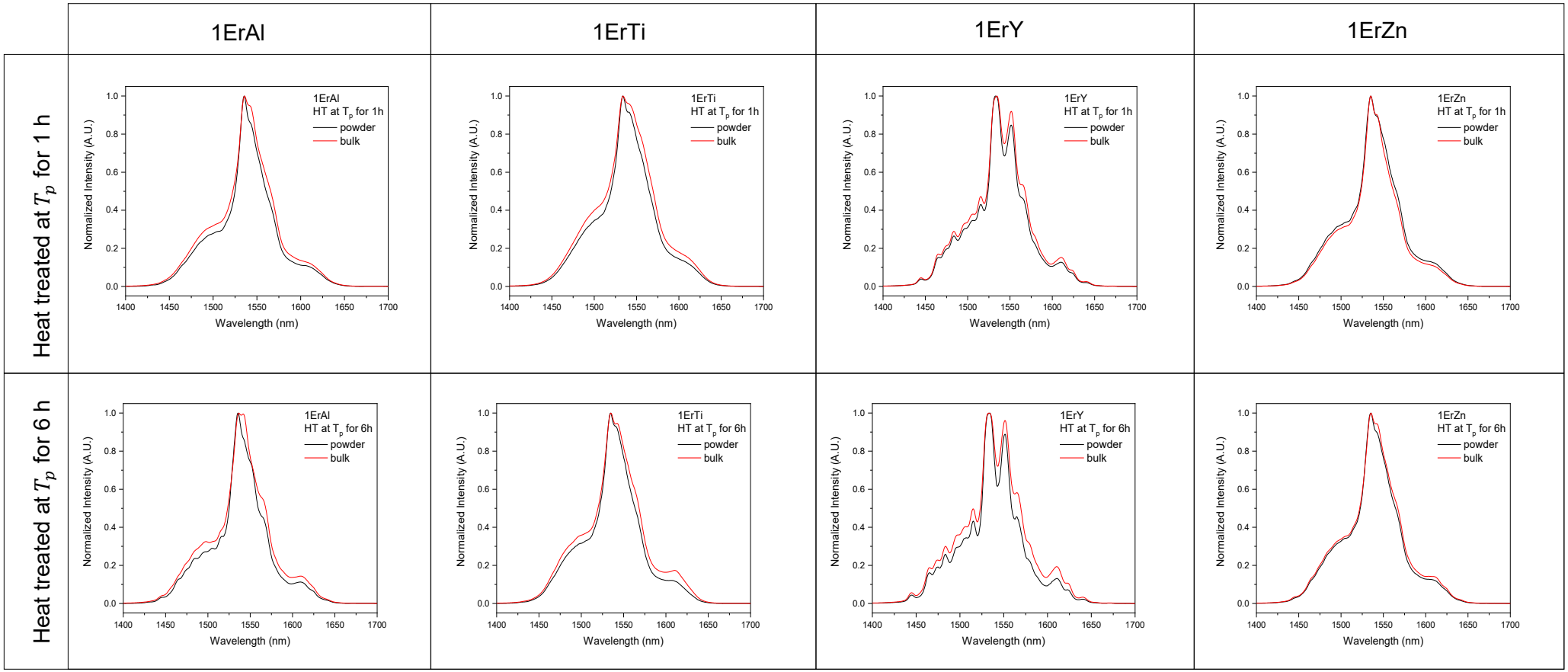

Figure 39. *Normalized intensity of the emission band at 1.5 μm under 976 nm excitation from the surface of bulk samples and from powdered samples.*

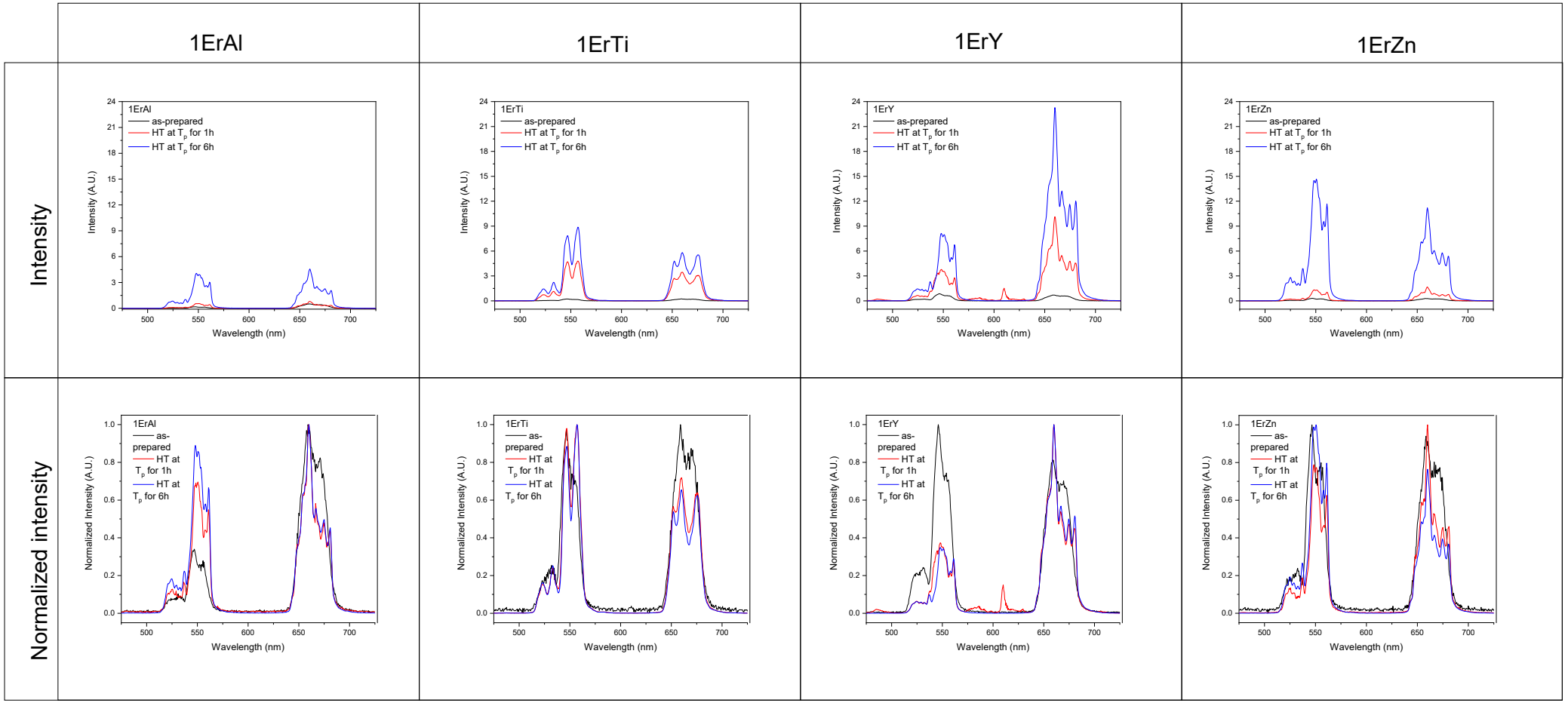

Figure 40. *Intensity and normalized intensity of the up-conversion emission under 976 nm excitation.*

While no change in the intensity of the emission at 2.7 μm was seen for the 1ErAl, 1ErTi and 1ErZn glasses after heat treatment, an increase in the intensity of the emission at 2.7 μm was detected after heat treating the 2.5ErY glass as seen in Figure 41.

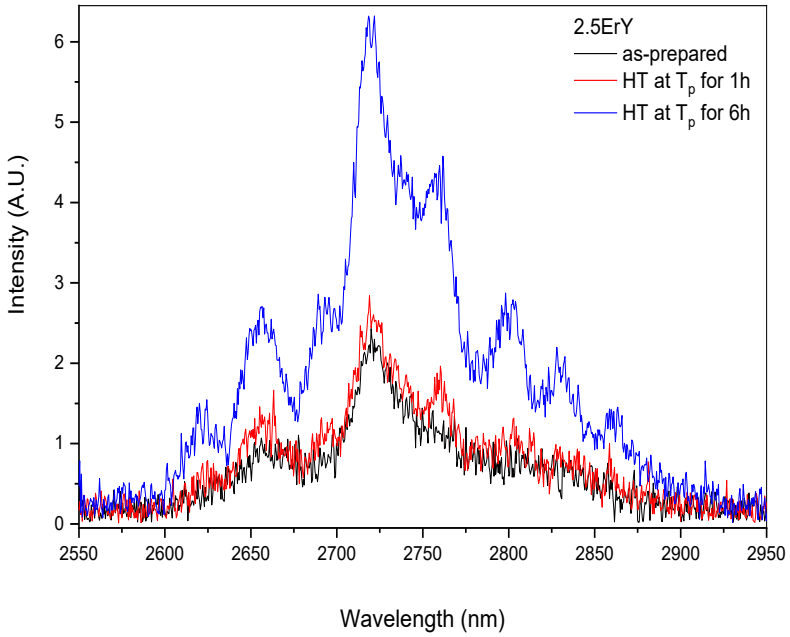

Figure 41. *The MIR emission spectra of the 2.5ErY samples under 976 nm excitation.*

Additionally, one can notice changes in the shape of the emission with the appearance of sharp peaks. The increase in emission and the change in the shape of the emission band is suspected to be due to the changes in the site of Er^{3+} ions after heat treatment. This clearly shows that the 2.5ErY glass is a promising glass for 2.7 μm applications.

According to the XRD analysis and by comparison of ionic radii of different cations present in the crystalline phases precipitated, it can be concluded that among all the crystals formed in the GCs, Y_2O_3 seems to be a good host for Er^{3+}. It has been shown that Er-doped Y_2O_3 crystals possess efficient NIR and MIR emission. Moreover, the emission spectra observed in GCs obtained from the Y-containing glasses are similar to MIR [76, pp. 56-58], NIR [77] and up-conversion [78] spectra reported for Er-doped Y_2O_3. Therefore, it may be concluded that Er^{3+} ions are incorporated in Y_2O_3 crystals upon devitrification of the Y-containing glass. This glass composition is the most promising for fabrication of Er-doped GC-materials for different applications among the compositions studied in this work.

4.2 Preliminary results on film deposition

A glass with the composition $64GeO_2$-$9.9Ga_2O_3$-$11.3BaO$-$8.9Na_2O$-$1Er_2O_3$-$5ZnO$ corresponding to the 1ErZn sample was prepared into a disk shape to be used as a target for the film deposition. A thin film of 25.2 nm thickness was deposited using electron beam deposition technique onto a fused silica substrate as described in Section 3.1.2.

The film was too thin to use SEM coupled with EDS to analyze its composition. Therefore, X-ray photoelectron spectroscopy (XPS) was used for the composition analysis. The XPS spectrum is shown in Figure 42.

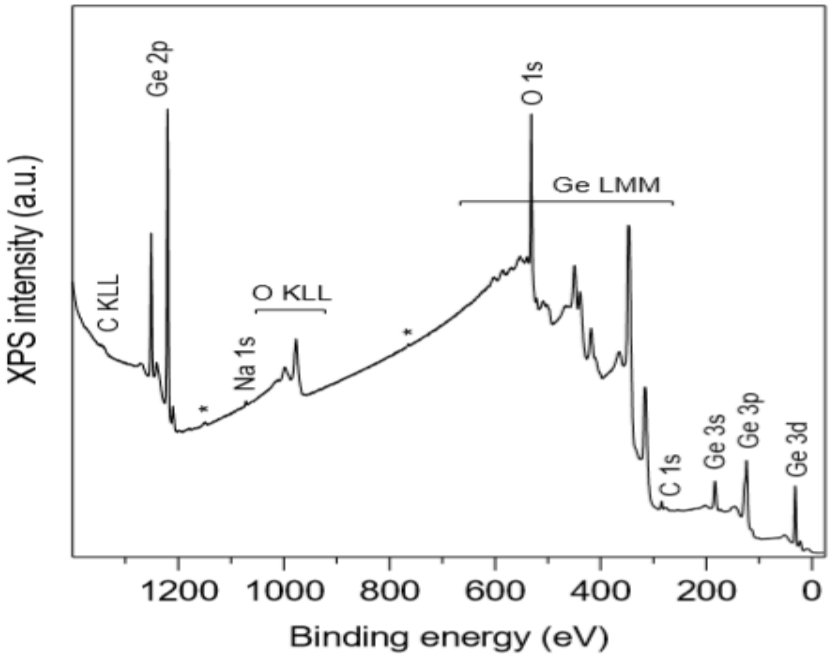

Figure 42. *Low resolution XPS spectrum measured from the thin film with the identified photoelectron peaks labeled.*

Surprisingly, only the signals from Ge and Na were detected. The composition of the film was estimated from the XPS spectrum. The relative surface concentration is given as

$$C_x = \frac{n_x}{\sum n_i} = \frac{\frac{I_x}{S_x}}{\sum \frac{I_i}{S_i}}, \tag{23}$$

where I_x is the number of photoelectrons per second for transition x, and S_x is the atomic sensitivity factor for the transition [54]. The atomic sensitivity factors are based on empirical data and corrected for the transmission function of the spectrometer. The results are presented in Table 9.

Table 9. *Surface concentration in atomic percentage of different elements in the thin film.*

Element and transition	**Sampling depth (nm)**	**Surface concentration (at. %)**
C 1s	6.8	9.45
O 1s	5.7	68.92
Na 1s	3.2	0.64
Zn 2p	3.4	-
Ga 2p	2.9	-
Ge 2p	2.4	20.99
Ba 3d	4.6	-
Er 4d	7.3	-

According to the analysis, the thin film consists mainly of GeO_2 indicating that the thin film has a different composition than the original target and the deposited film is not suitable for the application. It is therefore crucial to try new deposition using different parameters.

5. CONCLUSIONS

In this thesis, erbium doped germanate glasses and glass-ceramics of the composition $\left(1-\frac{x}{100}\right)$*(64.6$GeO_2-10Ga_2O_3$-11.4BaO-9Na2O)-x$Er_2O_3$-5MO with MO=$Al_2O_3$, TiO_2, Y_2O_3 and ZnO and with x=0, 1 and 2.5 (in mol%) were prepared and characterized in order to deposit a film with strong emission at 2.7 µm.

DTA was used to determine the thermal properties of the glasses. The 1ErY glass had the highest T_g and 1ErZn glass the lowest T_g indicating the strongest and weakest glass networks among the glasses, respectively. All of the glasses were deemed to have great thermal stability which is promising for thin film deposition of the glasses as no crystallization is expected during the process. The density of the glasses aligned with the increasing molar mass of the introduced elements. Raman and FTIR spectroscopies were used to study the structure of the glasses. The Al containing and Zn containing glasses were deemed to be the most and least polymerized among the glasses, respectively. The Y containing glass was considered to have the most packed glass network, due to higher number of 3-membered GeO_4-rings. Y and Ti are suspected to participate in forming the glass network. The OH content in the glasses was also determined from IR transmittance spectra. The glasses have a high OH content which can lower their 2.7 µm emission intensity due to energy transfer to OH groups. The 1ErY had the lowest OH content among the glasses, likely due to it having the most packed network. The optical properties of the glasses were studied by UV-VIS-NIR absorption, luminescence measurements and Judd-Ofelt analysis. The absorption cross-sections were similar among the glasses indicating that the site of Er^{3+} is not greatly affected by the change in composition as confirmed from the similar shape of various emission bands from the glasses. Judd-Ofelt analysis deemed the 1ErY to have the highest rigidity among the glasses, the analysis conformed the possibility for achieving efficient IR, green, red emissions under suitable excitation. No MIR emission could be measured from the 1 mol% Er_2O_3 containing glasses probably due to the large OH content in the glass and low Er_2O_3 content. New glasses were prepared with 2.5 mol% Er_2O_3, all the glasses showed an emission band at 2.7 µm under 976 nm pumping and can be considered promising materials for MIR emission. The intensity of 2.7 µm emission aligned with the OH content with 2.5ErY having the highest emission intensity and lowest OH content.

Then 1Er and 2.5Er glasses were heat treated at T_g+20°C for 17 h and followed by a hold at T_p for 1 h or 6 h to form glass-ceramics. The glasses had a ceramic appearance after heat treatment confirming that crystallization occurs upon heat treatment. The crystals of 1Er samples were studied by XRD, all of the glasses had multiple crystals precipitating during the heat treatment, the composition of which depended on the glass composition. A decrease in intensity of emission at 1.5 μm was evidenced for the 1ErAl, 1ErTi and 1ErZn samples, the decrease in emission was related to decrease in the distance between RE -ions. The Er^{3+} ions that are not incorporated in the crystals are forced into a smaller volume leading to clustering. The 1ErY glass had an increase in emission along with sharp peaks in the emission band, suggesting that some Er^{3+} ions are located in crystals and/or the site distribution of the Er^{3+} ions is reduced after heat treatment. Up-conversion spectra measurements further confirmed above conclusions about the changes in the Er^{3+} site in 1ErY glass and shortened distances between RE -ions for the other glasses. An increase in MIR emission along with sharp peaks in the emission band were detected after heat treating the 2.5ErY glass. This was suspected to be due the changes in the site of the Er^{3+} ions. It is suggested that Er-ions enter into Y_2O_3 crystals on Y^{3+} site based on the emission spectra of Er:Y_2O_3 crystals [76-78].

Thin film deposition trials were performed and preliminary results on thin film deposition of the glasses were presented. A target for thin film deposition of the composition 64GeO_2-9.9Ga_2O_3-11.3BaO-8.9Na_2O-1Er_2O_3-5ZnO corresponding to the 1ErZn sample was prepared. A thin film of 25.2 nm thickness was deposited using electron beam physical vapor deposition onto a fused silica substrate. The composition of the film was analyzed using XPS and only the signals from Ge and Na were detected clearly showing the need to continue the trials on film deposition

To conclude, 2.7 μm emission under 976 nm excitation was demonstrated in erbium containing germanate glasses and glass-ceramics. The Y containing glasses were considered the most promising material due to the highest MIR emission intensity, likely due to the most packed network and therefore lowest OH content. The emission at 2.7 μm can be further increased by heat treating and devitrification of the glass.

Future study should focus on varying deposition parameters or using different deposition technique to deposit thin film with MIR luminescent properties and similar composition as the target. Future effort should also be focused on OH reduction in order to increase the intensity of the MIR emission. The OH content could be decreased by melting the glass in a O_2 rich atmosphere, or by oxygen bubbling the melt [49] [79]. The final step

would be to further tailor the glass composition to achieve transparent glass-ceramics with Er^{3+} containing crystals and deposit these glass-ceramics to thin films.

REFERENCES

[1] Ambient (outdoor) air pollution, World Health Organization, 2018, website, Available (accessed on 24.4.2020): https://www.who.int/en/news-room/fact-sheets/detail/ambient-(outdoor)-air-quality-and-health

[2] S. D. Jackson, Towards high-power mid-infrared emission from a fiber laser, Nature Photonics, Vol. 6, 2012, pp. 423-431

[3] C. Charlton, M. Giovannini, J. Faist, B. Mizaikoff, Fabrication and Characterization of Molecular Beam Epitaxy Grown Thin-Film GaAs Waveguides for Mid-Infrared Evanescent Field Chemical Sensing, Analytical Chemistry Vol. 78, 2006, pp. 4224-4227

[4] M. Sieger, B. Mizaikoff, Toward On-Chip Mid-Infrared Sensors, Analytical Chemistry, Vol. 88, 2016, pp. 5562-5573

[5] H. Adachi, K. Wasa, Thin Films and Nanomaterials in Handbook of Sputter Deposition Technology Fundamentals and Applications for Functional Thin Films, Nano-Materials and MEMS, William Andrew, 2012, 660 p.

[6] Y. Tian, B. Li, R. Chen, J. Xia, X. Jing, J. Zhang, S. Xu, Thermal stability and 2.7 μm spectroscopic properties in Er^{3+} doped tellurite glasses, Solid State Sciences, Vol. 60, 2016, pp.17-22

[7] M. Yamane, Y. Asahara, Glasses for Photonics, Cambridge University Press, Cambridge, 2000, 284 p.

[8] M. C. Gonçalves, L. Santos, R. Almeida, Rare-earth-doped transparent glass-ceramics, Comptes Rendus Chimie Vol. 5, 2002, pp. 845–854

[9] J. fan, X. Yuan, R. Li, H. Dong. J. Wung, L. Zhang, Intense photoluminescence at 2.7 μm in transparent Er^{3+}:CaF_2-fluorophosphate glass microcomposite, Optics Letters, Vol. 36, No. 22, 2011

[10] R. Reisfeld and C. K. Jùrgensen, Excited State Phenomena in Vitreous Materials, Handbook on the Physics and Chemistry of Rare Earth 9, ed. K. A. Gschneidner Jr. and L. Eyring, 1987

[11] S. Kang, X. Xiao, Q. Pan, D. Chen, J. Qiu, G. Dong, Spectroscopic properties in Er^{3+} doped germanotellurite glasses and glass-ceramics for mid-infrared laser materials, Scientific Reports, Vol. 7, 2017

[12] W. H. Zachariasen, The atomic arrangement in glass, Journal of the American Chemical Society, Vol. 54, No. 10, 1932, pp. 3841-3851

[13] B. E. Waren, The Basic Principles Involved in the Glassy State, Journal of Applied Physics, Vol. 13, Iss. 602, 1942

[14] J.E. Shelby, Introduction to glass science and technology, Royal Society of Chemistry, Cambridge, 2005, 291 p.

[15] F. Gan, L. Xu, Photonic Glasses, World Scientific Publishing Co. Pte. Ltd, 2006, 447 p.

[16] G. R. Gordon, The LASER, Light Amplification by Stimulated Emission of Radiation, In Franken, PA and Sands, RH (Eds.). The Ann Arbor Conference on Optical Pumping, the University of Michigan, 1959

[17] C. Anderson, P. Taylor, C. Anderson, Rare Earth Flotation Fundamentals: A Review, American Journal of Engineering Research, Vol. 6, Iss. 11, 2017

[18] Y. Xia, L. Zhang, X. Shen, W. Wei, A significant enhancement of middle infrared fluorescence and up-conversion of Er^{3+} -doped transparent germinate glasses containing LaF_3 nanocrystals, Physica B: Condensed Matter, Vol. 554, 2019, pp.137-143

[19] P. L. Higby, I. D. Aggarwal, Properties of barium gallium germinate glasses, Journal of Non-Crystalline solids, Vol. 163, 1993, pp. 303-308

[20] J. Zhang, Y. Lu, M. Cai, Y. Tian, F. Huang, Y. Guo, S. Xu, 2.8 μm emission and OH quenching analysis in Ho^{3+} doped fluorotellurite-germanate glasses sensitized by Yb^{3+} and Er^{3+}, Scientific Reports Vol. 7, Iss. 1, 2017

[21] T. Wei, F. Chen, Y. Tian, S. Xu, Efficient 2.7 μm emission and energy transfer mechanism in Er^{3+} doped Y_2O_3 and Nb_2O_5 modified germanate glasses, Journal of Quantitative Spectroscopy & Radiative Transfer, Vol. 133, 2014

[22] M. Cai, B. Zhou, F. Wang, T. Wie, Y. Tian, J. Zhou, S. Xu, J. Zhang, R_2O_3 (R=La,Y) modified erbium activated germanate glasses for mid-infrared 2.7 μm laser materials, Scientific Reports, Vol. 5, 2015

[23] G. Bai, L. Tao, K. Li, L. Hu. Y. H. Tsang, Enhanced light emission near 2.7 μm from Er–Nd co-doped germanate glass, Optical Materials, Vol. 35, 2013, pp. 1247-1250

[24] M. Mortier, Between glass and crystal: glass-ceramics, a new way for optical materials, Philosophical Magazine B, Vol. 82, No. 6, 2002, pp. 745-753

[25] S. Karthika, T. K. Radhakrishnan, P. Kalaichelvi, A Review of Classical and Non-classical Nucleation Theories, Crystal Growth & Design, Vol. 16, Iss. 11, 2016, pp. 6636-6681

[26] R. W. Hopper, Stochastic theory of scattering from idealized spinodal structures: II, Scattering in general and for the basic late stage model, Journal of Non-Crystalline Solids, Vol. 70, 1985

[27] P. M. Martin, Deposition Technologies: An Overview, Elsevier Inc., 2010

[28] R.K. Singh, J. Narajan, Pulsed-laser evaporation technique for deposition of thin films: Physics and theoretical model, Physical Review B, Vol. 41, Iss. 13, 1990, pp. 8843-8859

[29] E.D. McClanahan, N. Laegreid, Production of thin films by controlled deposition of sputtered material. In: Behrisch R., Wittmaack K. (eds) Sputtering by Particle Bombardment III. Topics in Applied Physics, Vol. 64, 1991

[30] R. J. Martín-Palma, A. Lakhtakia, Vapor-Deposition Techniques in Engineered Biomimicry, Elsevier, 2013, 496 p.

[31] K.S. SreeHarsha, Principles of Physical Vapor Deposition of Thin Films, Elsevier, Amsterdam, 2006, 1160 p.

[32] R. Morea, A. Miguel, J. M. Fernandez-Navarro, J. Gonzalo, J. Fernandez, R. Balba, Nanostructuring the Er3+ distribution in PbO-Nb2O5-GeO2 thin film glasses, Optimal Materials, Vol. 41, 2015

[33] C. B. de Araújo, L. R. P. Kassab, Enhanced Photoluminescence and Planar Waveguide of Rare-Earth Doped Germanium Oxide Glasses with Metallic Nanoparticles, in Glass Nanocomposites, Elsevier Inc., 2016

[34] K. H. Yoon, J. H. Kim, Structural analysis and luminescent study of thin zinc germanate doped with manganese, Thin Solid Films, Vol. 519, Iss. 5, 2010

[35] B. Xu, J. Hao, Q. Guo, J. Wang, G. Bai, S. Zhou, J. Qiu, Ultrabroadband near-infrared luminescence and efficient energy transfer in Bi and Bi/Ho co-doped thin films, Journal of Materials Chemistry C, Vol. 2, 2014

[36] I. Gordon, L. Rothman, C. Hill, R. Kochanov, Y. Tan, P. Bernath, M. Birk, V. Boudon, A. Campargue, K. Chance, et al. The HITRAN2016 molecular spectroscopic database. Journal of Quantitative Spectroscopy and Radiative Transfer Vol. 203, 2017, pp. 3-69.

[37] N. J. Harrick, Internal Reflection Spectroscopy, John Wiley & Sons Inc, New York, 1967, 327 p.

[38] D. Popa, F. Udrea, Towards Integrated Mid-Infrared Gas Sensors, Sensors, Vol. 19, Iss. 9, 2019

[39] Y. Chang, V. Paeder, L. Hvozdara, J. Hartmann, H. P. Herzig, Low-loss germanium strip waveguides on silicon for the mid-infrared, Optics Letters, Vol. 37, No. 14, 2012

[40] Y. Chang, P. Wägli, V. Paeder, A. Homsy, L. Hvozdara, P. van der Wal, J. di Francesco, N. f. de Rooij, H. P. Herzig, Cocaine detection by a mid-infrared waveguide integrated with a microfluidic chip, Lab Chip, Vol. 12, Iss. 17, 2012, pp. 3020-3023

[41] S. E. Plunkett, S. Propst, M. S. Braiman, Supported planar germanium waveguides for infrared evanescent-wave sensing, Applied Optics, Vol. 36, Iss. 18, 1997

[42] A.B. Spierings, M. Schneider, Comparison of density measurement techniques for additive manufactured metallic parts, Rapid Prototyping Journal, Vol. 17, Iss. 5, 2011, pp. 380-386

[43] A. Marotta, A. Buri, F. Branda, Nucleation in glass and differential thermal analysis, Journal of Materials Science, Vol. 16, 1981, pp. 341-344

[44] P. J. Haines, Principles of thermal analysis and calorimetry, The Royal Society of Chemistry, Cambridge, 2002, 280 p.

[45] J.G. Solé, L.e. Bausá, D. Jaque, Fundamentals, An Introduction to the Optical Spectroscopy of Inorganic Solids, John Wiley & Sons, Ltd, 2005, pp. 1-38

[46] J. M. Hollas, Modern Spectroscopy, John Wiley & Sons, 2004, 483 p.

[47] D. W. Ball, Theory of Raman Spectroscopy, Spectroscopy Vol. 16, no. 11, 2001, pp. 32-34

[48] R. Minnes, M. Nissinmann, Y. Maizels, G. Gerlitz, A. Katzir and Y. Raichlin, Using Attenuated Total Reflection– Fourier Transform Infra-Red (ATR FTIR) spectroscopy to distinguish between melanoma cells with a different metastatic potential, Scientific Reports, Vol. 7, 2017

[49] X. Feng, S. Tanabe and T. Hanada, Hydroxyl groups in erbium-doped germanotellurite glasses, Journal of Non-Crystalline Solids, Vol. 281, 2001, pp. 48-54

[50] B.R. Judd, Optical Absorption Intensities of Rare-Earth Ions, Physical Review, Vol. 127, No. 3, 1962

[51] G. S. Ofelt, Intensities of Crystal Spectra of Rare-Earth Ions, Journal of Chemical Physics, Vol. 37, 1962

[52] B. Bartolo, O. Forte, Advances in Spectroscopy for Lasers and Sensing, Springer in cooperation with NATO Public Diplomacy Division, 2006, 564 p.

[53] B. He, Two-Dimensional X-Ray Diffraction, John Wiley & Sons, 2009, 426 p.

[54] J. Moulder, W. Stickle, P. Sobol, K. Bomben, Handbook of X-ray Photoelectron Spectroscopy, Perkkin-Elmer Corporation, 1992

[55] C. Cushman, S. Chatterjee, G. Major, N. Smith, A. Roberts, M. Linford, Trends in Advanced XPS Instrumentation, ResearchGate, 2016

[56] K. Lahtonen, M. Lampimaki, P. Jussila, M. Hirsimaki, M. Valden, Instrumentation and analytical methods of an x-ray photoelectron spectroscopy–scanning tunneling microscopy surface analysis system for studying nanostructured materials, Review of Scientific Instruments, Vol. 77, 2006

[57] E. I. Kamitsos, Y. D. Yiannopoulos, M. A. Karakassides, G. D. Chryssikos, H. Jain, Raman and Infrared Structural Investigation of $xRb_2O,(1 - x)GeO_2$ Glasses, Journal of Physical Chemistry, Vol. 100, 1996, pp. 11755-11765

[58] G. S. Henderson, H. M. Wang, Germanium coordination and the germanate anomaly, European Journal of Mineralogy, Vol. 14, Iss. 4, 2002

[59] T. Fukushima, Y. Benino, T. Fujiwara, V. Dimitrov, T. Komatsu, Electronic polarizability and crystallization of K2O–TiO2–GeO2 glasses with high TiO2 contents, Journal of Solid State Chemistry, Vol. 179, 2006

[60] G.S. Henderson, M.E. Fleet, The structure of glasses along the Na2O-GeO2 join, Journal of Non-Crystalline Solids, Vol. 134, Iss. 3, 1991

[61] M. Ferraris, D. Milanese, C. Contardi, Q. Chen, Y. Menke, UV–Vis, FT-IR and EPR investigation on multi-component germano-silicate glasses for photonics, Journal of Non-Crystalline Solids, Vol. 347, 2004, pp. 246-253

[62] L. Baia, T. Iliescu, S. Simon, W. Kiefer, Raman and IR spectroscopic studies of manganese doped GeO2-Bi2O3 glasses, Journal of Molecular Structure, Vol. 599, 2001, pp. 9-13

[63] X. Wen, G. Tang, J. Wang, X. Chen, Q. Qian, Z. Yang, Tm3+ doped barium gallo-germanate glass single-mode fibers for 2.0 μm laser, Optics Express, Vol. 23, No. 6, 2015

[64] P. Lopez-Iscoa, L. Petit, J. Massera, D. Janner, N. G. Boetti, D. Pugliese, S. Fiorilli, C. Novara, F. Giorgis, D. Milanese, Effect of the addition of Al2O3, TiO2 and ZnO on the thermal, structural and luminescence properties of Er3+ -doped phosphate glasses, Journal of Non-Crystalline Solids, Vol. 460, 2017, pp. 161-168

[65] M. Digonnet, Rare-Earth-Doped Fiber Lasers and Amplifiers, Revised and Explained, CRC Press INC, 2001, 798 p.

[66] L. Gomes, M. Oermann, H. Ebendorff-Heidepriem, D. Ottaway, T. Monro, A. Librantz, S. D. Jackson, Energy level decay and excited state absorption processes in erbium-doped tellurite glass, Journal of Applied Physics, Vol. 110, 2011

[67] M. Cai, T. Wei, B. Zhou, Y. Tian, J. Zhou, S. Xu, J. Zhan, Analysis of energy transfer process based emission spectra of erbium doped germanate glasses for mid-infrared laser materials, Journal of Alloys and Compounds, Vol. 626, 2015, pp. 165-172

[68] W. T. Carnall, P. R. Fields, K. Rajnak, Electronic Energy Levels in the Trivalent Lanthanide Aquo Ions. I. Pr^{3+}, Nd^{3+}, Pm^{3+}, Sm^{3+}, Dy^{3+}, Ho^{3+}, Er^{3+}, and Tm^{3+}, Journal of Chemical Physics, Vol. 49, 1968

[69] M. Ennouri, L. Kuusela, I. Jlassi, B. Gelloz, L. Petit, H. Elhouichet, Impact of Ag2O Content on the Optical and Spectroscopic Properties of Fluoro-Phosphate Glasses, Materials, Vol. 12, 2019

[70] K. Xiao, Z. Yang, Thermal stability and optical transitions of Er3+/Yb3+ -codoped barium gallogermanate glass, Optical Materials, Vol. 29, 2007, pp. 1475-1480

[71] M. J. Weber, Probabilities for Radiative and Nonradiative Decay of Er^{3+} in LaF_3, Physical Review, Vol. 157, No. 2, 1967

[72] Y. Liu, X. Y. Liu, W. C. Wang, W. J. Zhang, Q. Y. Zhang, 2.7 μm emission in Er3+ doped glass-ceramics containing lutetium oxyfluoride nanocrystals, Optical Materials Express, Vol. 6, No. 9, 2016

[73] A. Jha, S. Shen, M. Naftaly, Structural origin of spectral broadening of 1.5-μm emission in Er^{3+}-doped tellurite glasses, Physical Review Vol. 62, No. 10, 2000

[74] J. Massera, M. Mayran, J. Rocherullé, L. Hupa, Crystallization behavior of phosphate glasses and its impact on the glasses' bioactivity. Journal of Materials Science, Vol. 50, 2015, pp. 3091-3102

[75] A. Szczodra, A. Mardoukhi, M. Hokka, N.G. Boetti, L. Petit, Fluorine losses in Er3+ oxyfluoride phosphate glasses and glass-ceramics, Journal of Alloys and Compounds, Vol. 797, 2019, pp. 797-803

[76] A. Joshi, The Er^{3+}:Y_2O_3 Ceramic System, Doctoral of Philosophy in Electrical Engineering thesis, University of California, Los Angeles, 2012

[77] E. E. Brown, U. Hömmerich, A. Bluiett, C. Kuccera, J. Ballato, S. Trivedi, Near-Infrared Upconversion Luminescence in Er: Y_2O_3 Ceramics under 1.5 μm Excitation, Journal of American Ceramic Society, Vol. 97, Iss. 7, 2014

[78] J. A. Capobianco, F. Vetrone, T. D'Alesio, A. Speghini, M. Bettinelli, Optical spectroscopy of nanocrystalline cubic Er: Y_2O_3 obtained by combustion synthesis, Physical Chemistry Chemical Physics, Vol. 2, Iss. 14, 2000

[79] J. Massera, A. Haldeman, J. Jackson, C. Rivero-Baleine, L. Petit, K. Richardson, Processing of Tellurite-Based Glass with Low OH Content, Journal of American Ceramic Society, Vol. 94, 2011, pp. 130-136

APPENDIX A:

Table 10. *The determined branching ratios for different transitions.*

SLJ	S'L'J'	β(%)	SLJ
	1ErAl		
$^4I_{13/2}$	$^4I_{15/2}$	1	$^4I_{13/2}$
$^4I_{11/2}$	$^4I_{15/2}$	0.87	$^4I_{11/2}$
	$^4I_{13/2}$	0.13	
$^4I_{9/2}$	$^4I_{15/2}$	0.65	$^4I_{9/2}$
	$^4I_{13/2}$	0.35	
$^4F_{9/2}$	$^4I_{15/2}$	0.88	$^4F_{9/2}$
	$^4I_{13/2}$	0.05	
	$^4I_{11/2}$	0.06	
	$^4I_{9/2}$	0.01	
$^4S_{3/2}$	$^4I_{15/2}$	0.67	$^4S_{3/2}$
	$^4I_{13/2}$	0.28	
	$^4I_{11/2}$	0.02	
	$^4I_{9/2}$	0.03	
	1ErTi		
$^4I_{13/2}$	$^4I_{15/2}$	1	$^4I_{13/2}$
$^4I_{11/2}$	$^4I_{15/2}$	0.87	$^4I_{11/2}$
	$^4I_{13/2}$	0.14	
$^4I_{9/2}$	$^4I_{15/2}$	0.67	$^4I_{9/2}$
	$^4I_{13/2}$	0.33	

$^4F_{9/2}$	$^4I_{15/2}$	0.89	$^4F_{9/2}$
	$^4I_{13/2}$	0.05	
	$^4I_{11/2}$	0.06	
	$^4I_{9/2}$	0.01	
$^4S_{3/2}$	$^4I_{15/2}$	0.67	$^4S_{3/2}$
	$^4I_{13/2}$	0.28	
	$^4I_{11/2}$	0.02	
	$^4I_{9/2}$	0.03	

1ErY

$^4I_{13/2}$	$^4I_{15/2}$	1	$^4I_{13/2}$
$^4I_{11/2}$	$^4I_{15/2}$	0.86	$^4I_{11/2}$
	$^4I_{13/2}$	0.14	
$^4I_{9/2}$	$^4I_{15/2}$	0.66	$^4I_{9/2}$
	$^4I_{13/2}$	0.34	
$^4F_{9/2}$	$^4I_{15/2}$	0.89	$^4F_{9/2}$
	$^4I_{13/2}$	0.05	
	$^4I_{11/2}$	0.06	
	$^4I_{9/2}$	-	
$^4S_{3/2}$	$^4I_{15/2}$	0.67	$^4S_{3/2}$
	$^4I_{13/2}$	0.28	
	$^4I_{11/2}$	0.02	
	$^4I_{9/2}$	0.03	

1ErZn

$^4I_{13/2}$	$^4I_{15/2}$	1	$^4I_{13/2}$

$^4I_{11/2}$	$^4I_{15/2}$	0.86	$^4I_{11/2}$
	$^4I_{13/2}$	0.14	
$^4I_{9/2}$	$^4I_{15/2}$	0.66	$^4I_{9/2}$
	$^4I_{13/2}$	0.35	
$^4F_{9/2}$	$^4I_{15/2}$	0.89	$^4F_{9/2}$
	$^4I_{13/2}$	0.05	
	$^4I_{11/2}$	0.06	
	$^4I_{9/2}$	0.01	
$^4S_{3/2}$	$^4I_{15/2}$	0.67	$^4S_{3/2}$
	$^4I_{13/2}$	0.28	
	$^4I_{11/2}$	0.02	
	$^4I_{9/2}$	0.03	